A processive rotary mechanism couples substrate unfolding and proteolysis in the ClpXP degradation machinery

Zev A. Ripstein[1,2†], Siavash Vahidi[1,2,3,4†], Walid A. Houry[1,4], John L. Rubinstein[1,2,5] and Lewis E. Kay[1,2,3,4]

[1]Department of Biochemistry, University of Toronto, Toronto, Ontario, M5S 1A8, Canada.

[2]The Hospital for Sick Children Research Institute, Toronto, Ontario, M5G 0A4, Canada.

[3]Departments of Molecular Genetics, University of Toronto, Toronto, Ontario, M5S 1A8, Canada.

[4]Department of Chemistry, University of Toronto, Toronto, Ontario, M5S 3H6, Canada.

[5]Department of Medical Biophysics, University of Toronto, Toronto, Ontario, M5G 1L7, Canada.

† Z.A.R and S.V contributed equally to this work

Abstract

The ClpXP degradation machine consists of a hexameric AAA+ unfoldase (ClpX) and a pair of heptameric serine protease rings (ClpP) that unfold, translocate, and subsequently degrade client proteins. ClpXP is an important target for drug development against infectious diseases. Although structures are available for isolated ClpX and ClpP rings, it remains unknown how symmetry mismatched ClpX and ClpP work in tandem for processive substrate translocation into the ClpP proteolytic chamber. Here we present cryo-EM structures of the substrate-bound ClpXP complex from *Neisseria meningitidis* at 2.3 to 3.3 Å resolution. The structures allow development of a model in which the cyclical hydrolysis of ATP is coupled to concerted motions of ClpX loops that lead to directional substrate translocation and ClpX rotation relative to ClpP. Our data add to the growing body of evidence that AAA+ molecular machines generate translocating forces by a common mechanism.

Introduction

Protein degradation plays a central role in cellular physiology, regulating the timing of cell division, controlling stress responses, and ensuring the timely removal of damaged or aberrantly folded proteins (1, 2). The ClpXP system is essential for protein degradation in bacteria and mitochondria and is a key regulator of cellular homeostasis, pathogenesis, and intracellular parasitism (3–5). It also serves as a model for understanding the structure and function of other ATP-dependant proteolytic systems. The ClpXP holoenzyme is composed of a hexameric AAA+ (ATPases Associated with diverse cellular Activities) unfoldase (ClpX) and a tetradecameric serine protease consisting of two heptameric rings (ClpP). Together, the ClpXP complex acts to unfold and degrade protein substrates (Figure 1A) (6). ClpXP is essential in bacteria, and consequently small molecules that disrupt either the protease (e.g. β-lactones (7), phenyl esters (8, 9)) or AAA+ unfoldase (e.g. ecumicin (10), lassomycin (11), rufomycin (12), dihydrothiazepines (13)), or mimic the interaction between the two (e.g. acyldepsipeptides [ADEPs] (14–16)) can kill cells, establishing ClpXP as a target for novel therapeutics against a range of different infectious diseases and cancers (17–21).

X-ray crystallographic studies of ClpP alone reveal a barrel-like structure with the protease rings stacked coaxially to form an enclosed degradation chamber that sequesters the fourteen Ser-His-Asp catalytic triads (22, 23), akin to the 20S proteasome (24, 25). Early negative-stain electron microscopy showed that one or two ClpX particles can bind co-axially to ClpP, creating a continuous central channel for substrates from ClpX to the degradation chamber of ClpP (26–28). Biochemical and X-ray crystallographic studies show that the axial entrances to the degradation chamber are gated by flexible N-terminal loops of ClpP that open upon the binding of ClpX or ADEPs, allowing substrates into the degradation chamber (29–31). Binding

of ClpX and ClpP is mediated by loops containing an Ile-Gly-Phe motif (IGF loops) on ClpX that dock into hydrophobic pockets on the apical interfaces of ClpP subunit pairs (32–34). N-terminal loops on ClpP also transiently interact with ClpX (33, 35, 36). However, the precise nature of these interactions and how they allow coordination of the activities of ClpX and ClpP remains unclear.

ClpX uses energy released by ATP hydrolysis to create a pulling force that unravels folded protein domains for translocation into the degradation chamber of ClpP (6). This unfolding activity relies on a series of highly conserved loops in ClpX. These loops include the 'RKH' loops that surround the ClpX entrance pore and recognize substrates for proteolysis (37), and a pair of "pore loops" in each protomer, termed pore-1 loop (GYVG motif) and pore-2 loop (RDV motif) (Figure 1 – figure supplement 1A) that line the axial channel of the ClpX ring (38). Bulky aromatic and aliphatic side chains of the pore loops transmit the pulling force to the substrate, leading to its unfolding. While the mechanism by which some AAA+ ATPases convert the chemical energy of ATP into a mechanical force that unfolds substrates was established recently (39–44), and structures of ClpP and ClpX in isolation have been determined (45–48), the absence of structures showing ClpXP in the process of unfolding substrate has prevented an understanding of the conformational changes that are necessary for substrate engagement, unfolding, and translocation in this system. ClpXP must undergo hundreds of ATP hydrolysis events to unfold and degrade a single protein, likely via a process involving hydrolysis of one nucleotide at a time, but the lack of structural information for a ClpXP holoenzyme has limited understanding of how unfolding and degradation are coupled. For example, it is not clear how the symmetry mismatch (49–51) between the pseudo-symmetric hexameric ClpX and the seven-fold symmetric ClpP affects both the binding and interaction of these two components.

Here we present cryo-EM structures of the ClpXP holoenzyme from the gram-negative pathogen *Neisseria meningitidis* engaged with a protein substrate. The ClpXP portion of the structure is at 2.3 to 3.3 Å resolution, allowing construction of a nearly complete atomic model of the complex. Our findings show how ClpX grips and translocates substrates into the degradation chamber through a cycle of ATP hydrolysis events involving both concerted motions of pore loops along the substrate, as well as motions of ClpX on the apical surface of ClpP. The data lead to a model for interactions between symmetry-mismatched ClpX and ClpP that enable continuous degradation of substrates as ClpX rotates relative to ClpP.

Results

ATP-dependent binding and degradation of GFP-SsrA by ClpXP

ClpX and ClpP from *N. meningitidis* were expressed separately in *E. coli* before purification with metal affinity chromatography and size exclusion chromatography (SEC). Degradation assays using green fluorescent protein bearing an eleven-residue SsrA tag (GFP-SsrA) (43) were performed to ensure that the heterologously expressed *N. meningitidis* (Nm) ClpX and ClpP proteins, when mixed, have the well-established activity of the ClpXP holoenzyme. The presence of ClpP or ClpX alone led to no loss of GFP-SsrA fluorescence relative to background bleaching in the GFP-alone control assay. ClpX, ClpP, and ATP were all necessary to degrade GFP-SsrA (Figure 1B), confirming that degradation of GFP-SsrA by ClpXP is ATP-dependent. As shown below and in previous work (33, 52–54), the presence of MgATP is required for tight binding between ClpX and ClpP. Therefore, for further structural studies, an E185Q Walker B mutant of NmClpX (ClpX-WB) was used to slow ATP hydrolysis and prolong the lifetime of the ClpXP complex. SEC was performed to probe the oligomeric state of each component and the formation

of the holoenzyme, confirming that ClpP behaves as an oligomeric species consistent with its well-known tetradecameric architecture (Figure 1C – blue trace). ClpX-WB eluted as a hexamer in the presence of 2 mM MgATP (Figure 1C – green trace). Incubation of ClpX-WB and ClpP in the presence of MgATP resulted in a pair of higher molecular weight SEC peaks that contain both ClpX and ClpP (Figure 1C – red trace and SDS-PAGE gel insert), presumably corresponding to singly and doubly capped ClpXP complexes, that show that the ClpX:ClpP complex can be readily reconstituted *in vitro* with the *N. meningitidis* enzyme.

To isolate a substrate-bound holoenzyme, ClpXP was incubated with GFP-SsrA in the presence of MgATP. SEC fractions corresponding to doubly capped ClpXP bound to GFP-SsrA (Figure 1–figure supplement 1B - denoted with a *) were applied to specimen grids and vitrified for cryo-EM analysis. Visual inspection of the micrographs, as well as 2D classification of particle images, showed doubly capped complexes (Figure 1-figure supplement 2). However, 2D classification showed multiple classes where the two ClpX rings have lower density than the ClpP region, and other classes with one ClpX ring having strong density and the other having weak density. An *ab initio* 3D map showed ClpP along with strong density for one ClpX ring and only weak and fragmented density for the other (Figure 1–figure supplement 2C). Inspection of the map revealed that the ClpX ring is offset and tilted relative to the ClpP symmetry axis (Fig 1D, Video 1). The poor density for the second ClpX hexamer is likely due to the lack of correlation between binding offsets of the two ClpX rings which leads to incoherent averaging of one of the ClpX rings in the map. Refinement of the intact map led to an overall resolution of 2.8 Å (Figure 1–figure supplement 2C), however the density for the better-resolved ClpX ring remained fragmented. Further local refinement and classification in cryoSPARC (55) improved the density for ClpX and revealed two distinct conformations, at 3.3 Å and 2.9 Å resolution

(Figure 1–figure supplement 2), hereafter referred to as Conformations A and B, respectively. Focused refinement of ClpP with D7 symmetry applied led to a map at 2.3 Å resolution (Figure 1–figure supplement 2).

Overall architecture of NmClpXP

Atomic models built into the cryo-EM maps showed that in both Conformations A and B, ClpX is positioned with an offset and is tilted relative to the seven-fold symmetry axis of ClpP (Figure 1D, Video 1). Nevertheless, a continuous channel for substrate spans the ClpX and ClpP rings. ClpP is in its active extended conformation (56), and closely resembles a published ADEP-bound crystal structure with an all atom RMSD of 1.04 Å (56). Even though the full-length constructs of ClpX included the zinc binding domains (residues 1-62), no density was found for these domains in either conformation, likely due to their flexibility.

Conformations A and B of ClpX both contained additional density along their axial channels, adjacent to the pore loops, likely from the GFP-SsrA substrate that co-eluted with ClpXP from the SEC column (Figure 1E and 1F - orange) (Figure 1 – Figure Supplement 1B). The substrate enters ClpX at an angle of ~15° relative to the ClpP symmetry axis, and is gripped by five of the six ClpX protomers arranged in a right-handed spiral, akin to other AAA+ ATPases in their substrate-bound conformations (39–44). The sixth protomer forms a disengaged "seam" that bridges protomers at the beginning and end of the spiral. In the description that follows we have labeled the protomers X1 through X6 corresponding to their position in the spiral (Figure 1F), and consider the configuration in which X1 is the disengaged "seam" protomer of Conformation A.

The main differences between Conformations A and B are within the protomer that adopts the bridging seam position, and where the seam is located relative to ClpP. In

Conformation A, protomer X1 is disengaged from substrate and in the seam position (Figure 1F left - dark blue) while in Conformation B protomer X6 is disengaged from substrate and in the seam position (Figure 1F right - yellow). However, these two seam positions are not equivalent: in Conformation A the seam is further from the apical surface of ClpP in what we designate as the "upper seam" (US) position (Figure 1D,F - dark blue), while in Conformation B, the seam is closer to ClpP in the "lower seam" (LS) position (Figure 1D,F - yellow).

The symmetry-mismatched interaction interface between ClpX and ClpP

ClpX IGF Loops: In both Conformations A and B of ClpXP, there is clear density for most of the IGF loops that extend from the ClpX ring towards the apical surface of ClpP (Figure 2A). In Conformation A, clear density is observed for only five of the six IGF loops, with weak density belonging to the IGF loop of the X6 protomer (white dotted line in Figure 2B left; Figure 2-figure supplement 1). In Conformation B, the density of the X6 IGF loop is significantly stronger than in Conformation A, so that all six of the IGF loops are accounted for (residues 264-274, Figure 2B, right; Figure 2C; Figure 2-figure supplement 1), with the loops binding six of the seven pockets on ClpP. In both Conformations A and B, the empty ClpP binding pocket is located between the X5 and X6 protomers of ClpX (Figure 2B). The lack of density for the IGF loop belonging to protomer X6 in Conformation A (Figure 2-figure supplement 1) is likely due to conformational flexibility and sub-stoichiometric binding of this IGF loop into the ClpP binding pocket.

All six IGF loops in ClpX adopt different configurations in Conformations A and B (Figure 2-figure supplement 1). The ClpX residues immediately following where the IGF loops contact ClpP (residues 275-280) show weak or no density, likely indicating flexibility. This property allows the IGF loops to accommodate movement of the ClpX protomers relative to

ClpP (Figure 2D-F), analogous to a set of springs. For instance, in Conformation A the X1 protomer is closer to the ClpP surface than in Conformation B and its IGF loop is thus compact in this state. In contrast, in Conformation B the loop is fully extended, allowing the X1 protomer to reach ~7 Å towards the top of the spiral to engage the substrate (Figure 2F; Figure 2-figure supplement 1). In this way the flexibility of the IGF loops accommodates the spiral arrangement of ClpX necessary to bind and unfold substrate, while maintaining contact with the planar ring of ClpP. Additionally, the IGF loops allow the X2 protomer to move laterally away from the ClpP pore while the X4 and X5 protomers move toward it to form a structure in which the ClpP and ClpX rings are displaced with respect to each other (Figure 2D-red arrow; Figure 2E).

ClpP N-terminal Gates: Degradation assays (31, 35, 57–59) have shown that ClpX can open the N-terminal gates of ClpP, and indeed in both Conformations A and B the gates are in the "up" state, forming ordered β-hairpins (Figure 2G; Figure 2-figure supplement 2). These β-hairpins closely resemble the conformation seen in the ADEP-bound structures of NmClpP (56) and are notably different from the disordered conformations observed in NmClpP when it is not bound to either ClpX or ADEP (Figure 2–figure supplement 2B). By forming ordered gates, ClpX binding creates a wide entrance pore with a diameter of ~23 Å for substrates to pass through into the ClpP degradation chamber (Figure 2G, left; Figure 2–figure supplement 2). While it has long been suspected that the activating mechanism of ADEPs involves a disorder-to-order transition of these gates (30), this observation provides direct evidence that ClpX creates the same effect.

In both Conformations A and B, the rigidification of the ClpP N-terminal gates varies substantially between protomers. At one extreme, the N-terminal residues of the ClpP protomer that is not bound to an IGF loop have the weakest density, appearing to possess the most flexibility at the top of the β-hairpin (Figure 2G center; Figure 2-figure supplement 2E). In

contrast, the N-terminal residues of the ClpP protomer proximal to the X5 ClpX protomer, are held rigidly through contacts with the ATPase (Figure 2G right). This interaction is mediated by a pair of α-helices from protomer X5 (residues 254-262 and 291-296) adjacent to the IGF loop, and by another X5 α-helix that precedes the pore-2 loop (residues 186-192). These three α-helices stabilize the β-hairpin structure of the ClpP N-terminal residues by interacting with Arg17 at the top of the hairpin (Figure 2E inset). These interactions are unique for the X5 protomer due to the lateral displacement of the ClpX ring relative to the axial pore of ClpP (Figure 2A), with the X2 protomer shifted furthest from the pore while the X5 protomer is pulled overtop of the pore (Figure 2D&F). Even without interacting directly with ClpX, the remaining five ClpP protomers have nearly rigid N-terminal gates, with reduced density only for residues located in the turn of the β-hairpin that likely reflects increased flexibility in this region (Figure 2-figure supplement 2F). Gate rigidification therefore appears to be mediated by an allosteric effect when IGF loops engage their respective ClpP binding pockets, akin to the effect observed upon ADEP binding (15, 30). In the ClpXP complex with substrate bound, only a single ClpX protomer (X5) interacts directly with a single ClpP gate at any given time. The mechanism of substrate translocation described below involves movement of the ClpX ring on the apical surface of ClpP, with each ClpX protomer forming contacts with a ClpP gate as translocation proceeds.

Substrate Engagement by ClpX

ClpX fits neatly into the emerging consensus for how AAA+ unfoldases engage substrate (39–43). In both Conformations A and B, five of the six pore-1 loops of ClpX interact tightly with the substrate backbone, with Tyr153 forming the majority of the interface (Figure 3A&B). These protomers generate a right-handed spiral that wraps around an 8 to 10 residue stretch of the

substrate along the central channel of ClpX (Figure 3C&D). In Conformation A, the X1 pore-1 loop in the US orientation is disengaged, with the X2 protomer at the top of the spiral. As the spiral continues downwards, protomers X3, X4, and X5 make contacts with the substrate. The spiral terminates with the X6 pore-1 loop that is engaged with the substrate closest to the ClpP apical surface (Figure 3C). In Conformation B, the X6 pore-1 loop is disengaged (LS orientation), while the X1 pore-1 loop engages a new section of substrate (Figure 3D) and the X5 protomer is now located closest to the ClpP surface. When transitioning between substrate-engaged and disengaged states, the X6 pore-1 loop undergoes a large conformational change (Figure 3E). As it disengages the substrate the "lasso" fold (Figure 3E, left) that allows Tyr153 and Val154 of pore 1 to point towards the substrate is replaced by a short α-helix immediately following the GYVG motif of the loop.

Interestingly, the X1 and X5 protomers make additional contacts with the substrate in Conformation B. Whereas all of the pore-2 loops from the other five protomers are radially removed and disengaged from the substrate, the X1 protomer extends its pore-2 loop residues Ile198 and Thr199 to engage the substrate at a position three or four residues down the substrate chain from where its pore-1 loop binds (Figure 3D&F). The RKH loops, located at the top of the ClpX ring (Figure 3–figure supplement 1), are highly conserved motifs among the ClpX family of AAA+ unfoldases and are known to contribute to substrate recognition (60–62). In Conformation B only the RKH loop of X5 directly engages substrate, with its His230 residue interacting at a position three or four residues up the substrate chain from where its pore-1 loop binds (Figure 3D&F). In order to contact substrate at this position the RKH loop of the X5 protomer rearranges to point toward ClpP (Figure 3F), in contrast to the other RKH loops which point away from the axial channel of ClpX (Figure 3-figure supplement 1). These five RKH

loops are located away from the substrate, and have weaker density in the maps, likely indicating flexibility.

Nucleotide State and Cycling in ClpX

The cryo-EM maps allowed unambiguous identification of the nucleotide bound to each ClpX protomer. In Conformation A, there is strong density for ATP and a magnesium cofactor in protomers X2, X3, X4, and X5, while the X1 and X6 protomers are ADP loaded, with no density for either the γ-phosphate or magnesium (Figure 4A,4C). As in both the classic and HCLR clades of AAA+ ATPases (39–43), the orientation between the large and the small AAA+ domains of ClpX changes considerably depending on the nucleotide state. In Conformation A, both the X1 and X6 protomers adopt conformations that allow the X1 protomer to move away from the pore in the US position (Figure 4-figure supplement 1) and there is reduced surface area buried between X1 and its neighboring protomers X2 and X6. In agreement with this finding, the local resolution in the cryo-EM maps (Figure 4-figure supplement 2) shows that the X1 protomer in the US position is significantly more flexible than the other protomers. In Conformation B only the X6 protomer is ADP-bound. The X1, X2, X3, X4, and X5 protomers are ATP-bound with clear density for the γ-phosphate and the magnesium cofactor (Fig 4B and D). Interestingly, the X5 protomer adopts a unique orientation between its large domain and small domain compared to the other ATP-bound protomers in order to accommodate the translation of the X6 protomer away from the substrate translocation channel into the LS position (Figure 4B orange box; Figure 4-figure supplement 1).

In Conformation A, the β- and γ-phosphates of the bound ATP are stabilized by interactions with the sensor-II arginine (Arg369) of the same subunit and the arginine finger (Arg306) from the adjacent clockwise protomer (Figure 4C). In the ADP-bound sites of the X1

and X6 protomers, both arginines have moved away, allowing for a more open nucleotide binding pocket (Figure 4C). In contrast, in Conformation B both the sensor-II arginine and the arginine finger contact the β and γ-phosphates in only four of the five ATP-bound protomers (X1, X2, X3, and X4) (Figure 4D). In the ATP-bound X5 protomer (at the bottom of the spiral), the adjacent X6 protomer and its arginine finger have pivoted away from the nucleotide into the LS position, allowing the sensor-II arginine to move closer to the γ-phosphate of the bound ATP. In addition, the Walker B motif moves closer to ATP presumably to prime this site for ATP hydrolysis. Notably, this key sensor II-priming motif in the primed nucleotide site has also been reported for the Lon protease bound to substrate (42), a close relative in the HCLR clade of AAA+ proteins.

Discussion

In this study we used cryo-EM to build atomic models of a ClpXP complex bound to a SsrA-tagged GFP substrate. Structures of a variety of different AAA+ rings with substrates have emerged in the past several years (39–43), providing a description of how these ATP-dependent molecular machines unfold clients. In addition, methyl-TROSY NMR studies of a VAT-substrate complex provided atomic-level insights into structural changes associated with the client as it is pulled into the lumen of the unfoldase (63). Nevertheless, a detailed understanding of how a pair of symmetry mismatched ClpP/ClpX rings can work in tandem to unfold, translocate, and subsequently degrade substrates in a processive manner has remained elusive. Our structural data suggest a translocation mechanism that can be explained in terms of a pair of conformers, denoted as Conformations A and B here, that represent two steps along the substrate translocation pathway (Figure 5A). To aid in the following discussion we have color-coded the

ClpX protomers and refer to them with their X1 - X6 labels. As we will discuss, each of these protomers will cycle between all six protomer positions along the spiral, including, among others, a state primed to hydrolyze ATP (denoted as ATP*) as well as the LS and US positions. This cycling is linked to ATP hydrolysis, to the attachment position of ClpX pore-loops along the substrate, and to the interaction of ClpX IGF loops with ClpP. We begin our discussion of the unfolding/translocation cycle with the X1 protomer in Conformation A in the US position, detached from substrate and bridging the lowest and highest positions of the ClpX spiral. Both X1 and X6 protomers are ADP-bound, while the remaining protomers are in ATP-bound states. In Conformation B, X1 moves to the highest position of the spiral with respect to substrate (compare Figure 2F, top and bottom panels) simultaneously exchanging ADP for ATP in its nucleotide binding pocket (Figure 5B). This transition brings X1 into close proximity with X2 and allows engagement of X1's pore loops with substrate. The X1 pore-l loop now sits at the top of the spiral, two substrate residues above the X2 pore loop (Figure 5A&B), thereby translocating additional residues of substrate into the unfoldase. This transition also leads to release of substrate by X6, which pivots away from the central pore to adopt the LS position (second ring, Figure 5A). ATP hydrolysis and phosphate release by X5, which was in the ATP-hydrolysis primed ATP* state, restores the ClpX spiral back to the Conformation A state, (third ring of the four in Figure 5A), with X6 now assuming the US position. The complex is thus reset so that it can take another step along the substrate during the next A to B transition (third ring to fourth ring in Figure 5A). The cumulative effect of these transitions is a cycling of ClpX protomers through different positions on the spiral (Figure 5A&B). For example, the protomer initially in the US position (X1 in our discussion) will, with each step, move along the spiral such that it transitions from the US position to the top of the spiral (Conformation B) and then

306 successively moving to lower spiral positions, through the ATP* state and finally the LS
307 position, as substrate is translocated. Each Conformation A→Conformation B→Conformation A
308 step results in the exchange of ADP for ATP and a single ATP hydrolysis event. Continuous
309 repetition of these steps leads to a processive "hand-over-hand" translocation of substrate
310 through the axial pore of ClpX into ClpP (Illustrated in Video 2).

311 The sequential hydrolysis of ATP at the ATP* position results in unidirectional substrate
312 translocation and movement of pore loops along the substrate (Figure 5B), with the counter
313 clockwise hydrolysis cycle translating into a repeated downward pulling force on the substrate.
314 Both the sequential hydrolysis of ATP as well as the "hand-over-hand" substrate pulling model
315 appear to be conserved for AAA+ unfoldases (39–43).

316 The cycle described above, in which each protomer eventually adopts all positions in the
317 spiral, has significant implications for how the IGF loops interact with the ClpP binding pockets.
318 If the spiral position of each ClpX protomer was independent of IGF binding, alignment of the
319 asymmetric ClpX spiral would lead to averaging of the IGF loops into all the pockets of ClpP
320 during cryo-EM map refinement. However, our structures clearly show an empty IGF pocket on
321 ClpP *only* between the ATP* and LS positions of Conformation B (Figure 2B), suggesting that
322 this pocket must undergo a "cycle" as well (Figure 5C). Thus, following ATP hydrolysis and
323 phosphate release, the IGF loop of the protomer in the ATP* position (X5 initially) must leave
324 its engaged pocket and move to bind the adjacent empty site on ClpP (red arrows in Figure 5C),
325 as the complex transitions back to Conformation A (third ring in Figure 5A). In this state, the
326 IGF loop appears not to have assumed a structure that allows for tight binding as only weak
327 density is observed for it in EM maps. In contrast, strong binding is observed for this loop in
328 Conformation B (Figure 4-figure supplement 1). Consistent with this model, the IGF loop of the

X5 protomer has an "extended/stretched" structure in the ATP* position of Conformation B (Figure 2F), which likely causes strain and facilitates loop release and subsequent binding to the corresponding site on the adjacent ClpP protomer (Figure 5C). After seven IGF loop release and reengagement events, accompanied by seven ATP hydrolysis steps, the 'empty' ClpP binding site makes a complete cycle, returning to its starting position (Figure 5C). The accompanying motion of ClpX on the apical surface of ClpP for a given IGF loop transition is complex and subtle, yet seven of these transitions lead to a net 60° rotation of ClpX with respect to ClpP (note the positions of the purple ClpX protomer in the first and seventh panels in Figure 5D; Video 3). The model described above is the simplest one that is consistent with our data. More complicated models can be envisioned. For example, if each upward step of a ClpX protomer was not coupled to IGF loop displacements, or relative motion of ClpX on the apical surface of ClpP, additional states would have to be invoked, for which no experimental data has been observed.

During preparation of this manuscript two preprint manuscripts reported structures of ClpXP from *L. monocytogenes* (64) and from *E. coli* (65), with ClpX resolutions ranging from 3.9 to 6 Å. While density maps and atomic models are not available for direct comparison with the NmClpXP, a few important similarities and differences are notable. In all species, the ClpX ring appears to adopt a similar offset relative to the symmetry axis of ClpP, indicating that the general architecture of the ClpXP machinery is conserved. Notably, however, the N-terminal apical loops of *L. monocytogenes* ClpP are not rigidified upon ClpX binding (64), in contrast to the observation here that the gates rigidify upon binding to create a pore for substrate entry. Additionally, substrate engagement is different between the ClpXP from *N. meningitidis* described here and from *E. coli* (65). In the Conformation A seen with *N. meningitidis*, there is no engagement of substrate by any of the six pore-2 or six RKH loops, while in Conformation B

only a single RKH loop and a single pore-2 loop contact substrate (Figure 3D&F). This observation is in contrast to the recently reported *E. coli* ClpXP structures (65) in which arginines located in the pore-2 loop from three to five different protomers (depending on the structure), as well as multiple RKH loops, form major contacts with substrate. The differences in these interactions may reflect the fact that while pore-1 loop motifs are critical for forming interactions with client and in providing the force for translocation, additional contacts may differ between species and may be necessary for recognition of degradation signals and for substrate specificity.

Although in the ClpXP structures from *E. coli* (65) the ClpX ring adopts the same spiral staircase arrangement observed in many AAA+ ATPases (39–43, 66, 67), strongly supporting the "hand-over-hand" mechanism of substrate translocation, the authors of this work instead posit a stochastic mechanism (65, 68) for the HCLR clade of ATPases based on the observation of only a single bound ADP in their structures. In the stochastic model only a single protomer pulls the substrate, via a state that has yet to be observed. Such a model, involving stochastic nucleotide hydrolysis, appears inconsistent with the observations here and for the related Lon protease (42) where two neighbouring protomers are bound with ADP. It also appears to be in conflict with studies of the VAT AAA+ unfoldase (43) whereby nucleotide hydrolysis was shown to occur in a cycle that could be disrupted through the substitution of a single hydrolysis-impaired protomer into the ATPase ring. In contrast, the identification of two conformations in the *N. meningitidis* enzyme and observations of the bound nucleotides in each ClpX protomer leads to a simple model of cyclic hydrolysis that, in turn, results in unidirectional substrate translocation. In this model, the substrate is always gripped by multiple protomers, with only a single protomer disengaged as it traverses from the bottom to the top of the spiral. While unique

375 features will undoubtedly continue to emerge regarding subtle functional aspects of different
376 AAA+ unfoldases it is likely that the translocating forces generated by these molecular machines
377 are based on a common mechanism.

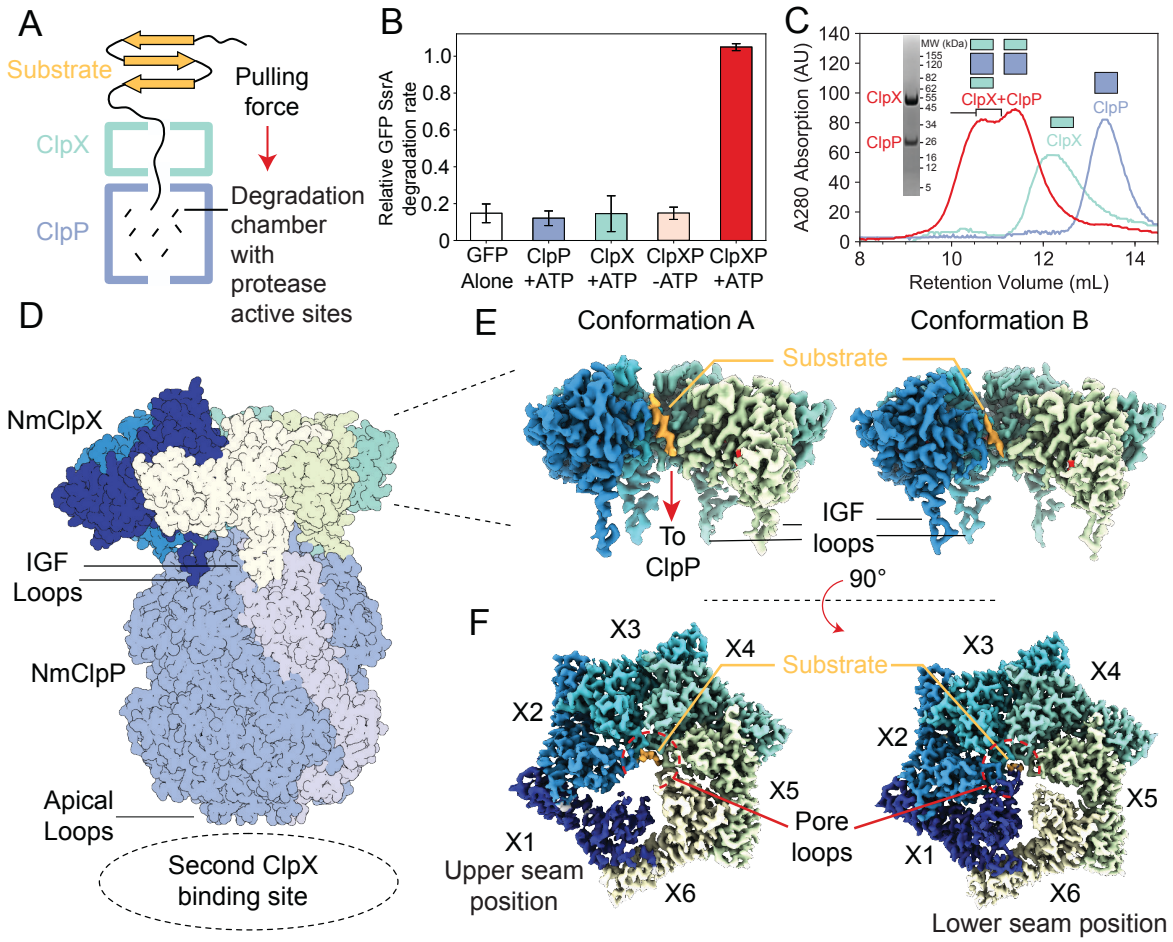

Figure 1. Functional and structural characterization of ClpXP from *N. meningitidis*. (A) Schematic representation of the ClpXP degradation machinery. The overall positions of the substrate (orange), ClpX unfoldase (green), and the ClpP protease (blue) are shown; (B) GFP-SsrA degradation by ClpXP is ATP-dependant. The degradation rate of GFP-SsrA is monitored by measuring loss of fluorescence. The components (ClpX, ClpP, ATP) included for each measurement are denoted on the plot. All measurements included GFP-SsrA and were performed in triplicate; (C) ClpXP complex formation monitored by size exclusion chromatography (SEC). SEC profiles of isolated ClpP (blue trace) and ClpX (green trace) are consistent with their expected molecular weights. SEC profile of a 2:1 $ClpX_6$:$ClpP_{14}$ mixture (red trace) incubated for 10 minutes in the presence of MgATP shows the formation of doubly- and singly-capped ClpXP complexes. The running buffer for all traces contained 2 mM MgATP. SDS-PAGE gel of SEC fractions shows that they contain both ClpP and ClpX; (D) Overall architecture of the ClpXP complex as established by cryo-EM. The ClpP double ring component is shown in dark blue, with the exception of a pair of opposing protomers shown in light blue shade to delineate the IGF loop binding site that is located at the interface between protomers. Cutaway side (E) and top (F) views of Conformations A and B of ClpX resulting from focused classification and local refinement. The IGF loops that bind to ClpP, and the presence of substrate (orange) in the axial channel of ClpX, are highlighted. Each of the ClpX protomers is labeled. In panel (F), the engagement of the substrate (orange) with five of the six pore loops is indicated (red semi-circle).

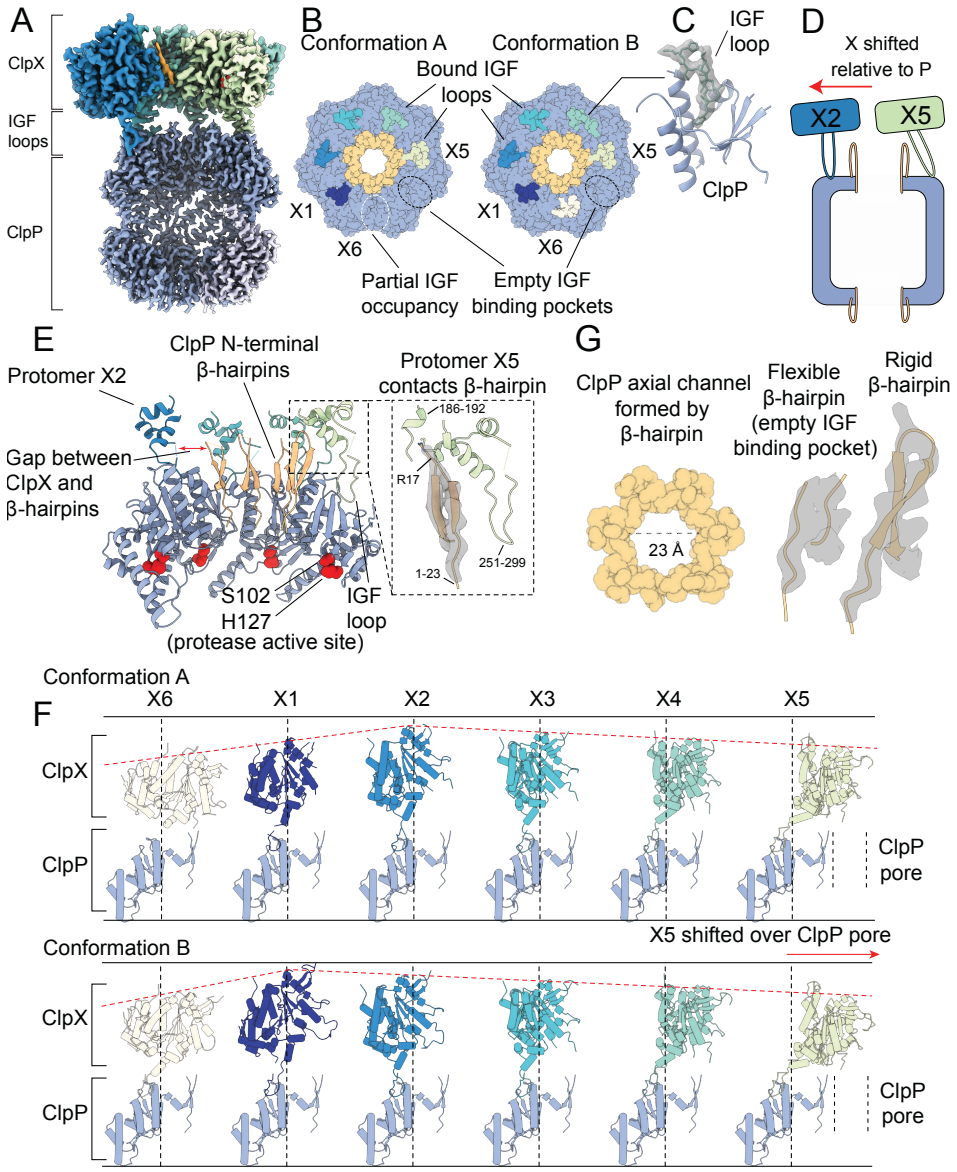

Figure 2: The interaction interface between ClpX and ClpP. Protomer X1 occupies the US position in Conformation A and protomer X6 the LS position in Conformation B. (A) Cutaway density map of the overall architecture of the ClpXP interaction interface. (B) Models for the ClpP apical surface and the ClpX IGF loops (residues 265-275). The empty IGF binding pocket (dotted oval) resides clockwise to the X5 protomer in both conformations. In Conformation A an IGF loop was not built into the map for protomer X6 due to weak loop density (yellow dotted line). (C) Model in map fit for an IGF loop (grey), surrounded by regions of ClpP comprising the IGF binding site (blue). (D) Interaction of the ClpP N-terminal gates with ClpX. The X2 protomer moves away from the gates, while the X5 protomer directly contacts the gate of the ClpP protomer to which its IGF loop is bound, shown schematically in (E). Inset shows the details of this interaction, with model in map fit for the ClpP β-hairpin. (F) Positions of ClpX protomers relative to ClpP. Images were generated by fitting all ClpP protomers to a common protomer and displaying the corresponding ClpX protomer. In both conformations ClpX adopts a spiral arrangement relative to ClpP (dotted red line). In Conformation A, the X2 protomer is located at the top of the spiral, while in Conformation B the X1 protomer occupies the top position, ~7 Å higher than its position in Conformation A. The ClpX protomers rotate and translate relative to ClpP; protomers X2 and X3 sit nearly atop their ClpP protomers, while X4 and especially X5 show large deviations from this position (vertical lines), with X5 sitting overtop the ClpP axial pore. (G) View down the channel formed by the N-terminal ClpP β-hairpins (left); density and models for the most flexible and rigid β-hairpins (center & right, respectively).

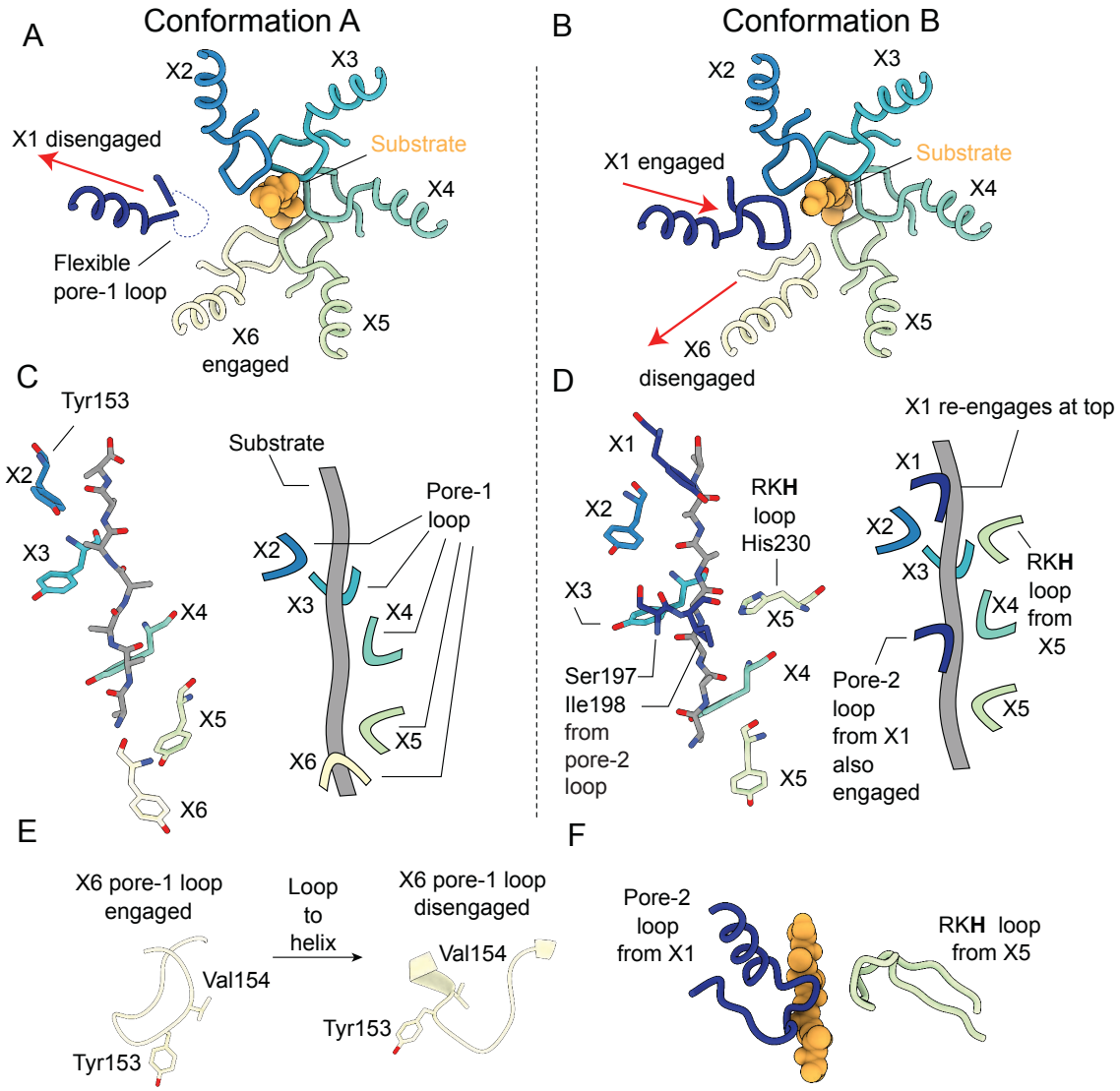

Figure 3. Substrate engagement by the ClpX pore loops. (A and B) Pore-1 loop residues grip the substrate, as observed in this view looking down the axial channel. The substrate is modelled as poly-Ala. (A) In Conformation A, the X1 protomer is disengaged from the substrate in the US position (red arrow) and shows noticeable flexibility in its pore-1 loop. (B) In Conformation B the X1 protomer contacts the substrate but the X6 protomer has disengaged into the LS position (red arrows). (C and D) Model of substrate and interacting residues, along with schematic, viewed perpendicular to the axial channel. (C) In Conformation A only the Tyr153 residue of the pore-1 loop makes significant contacts with the substrate; the 5 protomers (X2, X3, X4, X5, X6) form a downward spiral surrounding the backbone of the substrate chain, extending to the apical surface of ClpP. (D) In Conformation B, in addition to the five Tyr153 residues from the 5 gripping protomers (X1, X2, X3, X4, X5), more contacts are formed: Ser197 and Ile198 from the pore-2 loop of the X1 protomer and His230 from the RKH loop of the X5 protomer. (E) Substrate induced conformational changes of the X6 pore-1 loop upon releasing client. When the X6 protomer is substrate engaged its pore-1 loop forms a lasso like conformation, with Tyr153 and Val154 both pointing towards the axial channel (left). When disengaged, a part of the pore-1 loop becomes an α-helix, with Val154 and Tyr153 no longer pointing outwards (right). (F) Architecture of the additional contacts made by the pore-2 and RKH loops from the X1 and X5 protomers, respectively.

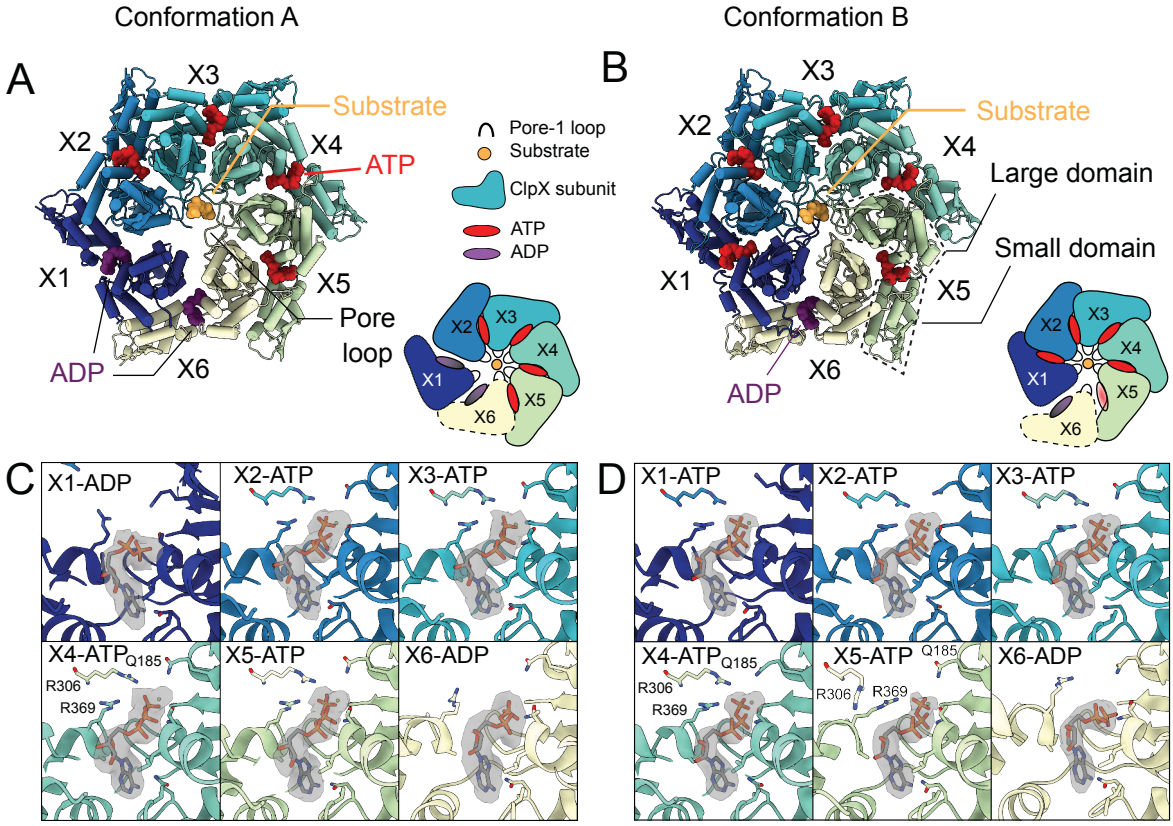

Figure 4. Nucleotide occupancy and interactions with ClpX. (A&B) Model of ClpX in conformations A and B, looking into the ClpX pore. Nucleotides are shown and color-coded, with ATP red and ADP purple, and bind between the large and small domains (boxed). Inset shows a schematic of the protomer positions and nucleotide occupancies. Conformation A has two bound ADP, in the X1 (dark blue, US in Conformation A in this representation) and X6 (yellow, LS in Conformation B in this representation) protomers, with the X1 protomer disengaged from the substrate and away from the axial pore (US position). In Conformation B only a single ADP is bound, protomer X1 is reengaged with substrate and X6 has disengaged. (C) Nucleotide binding sites of Conformation A, with key interacting residues shown along with the experimental density maps corresponding to bound nucleotide. In the ADP bound sites, both the arginine finger (R306) and the sensor-II arginine (R369) have moved away, while in the ATP bound sites they form close contacts with the β and γ-phosphates. (D) Nucleotide binding in Conformation B. As in Conformation A, R306 and R369 have moved away from the ADP, while in the X5 protomer only the arginine finger has moved away, while the sensor-II transitions closer to the γ-phosphate.

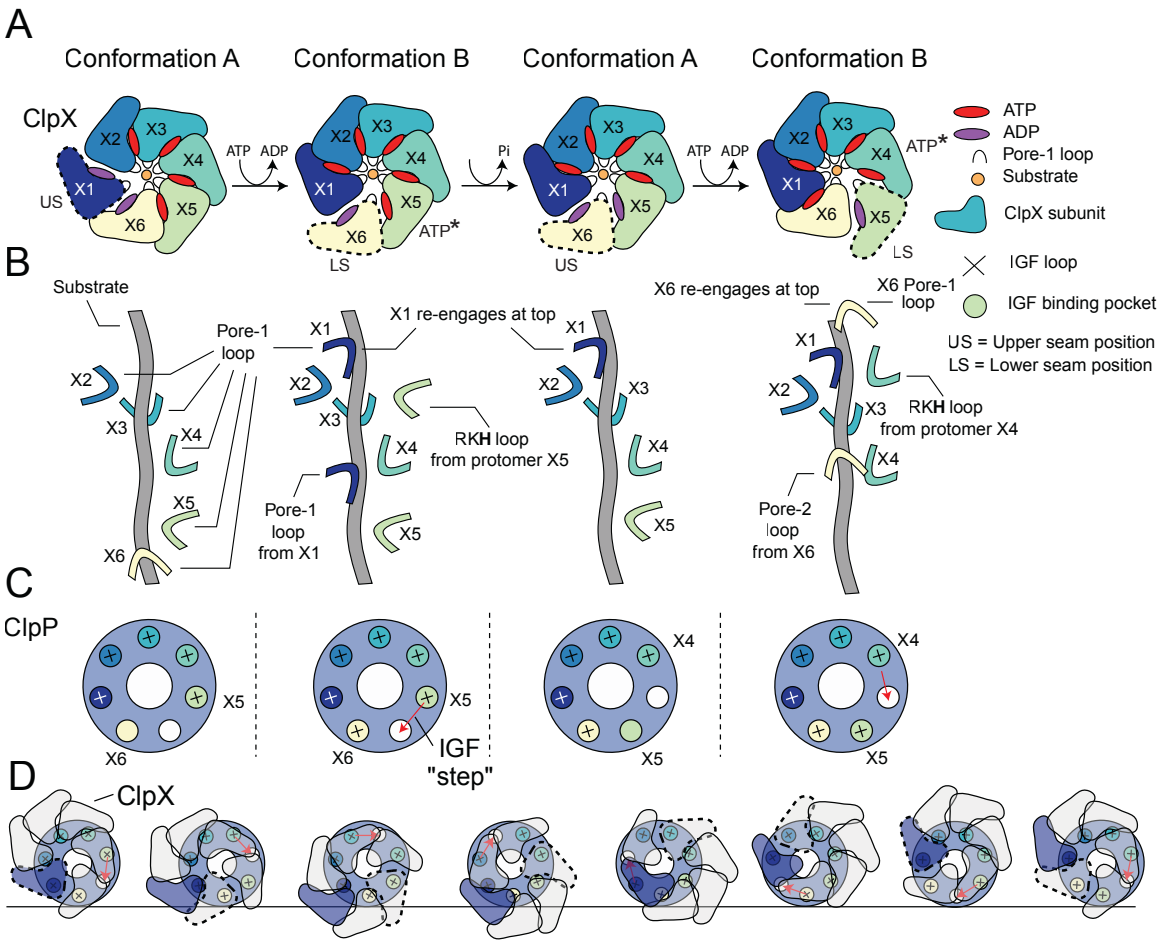

Figure 5. Translocation model for ClpXP. (A) Schematic of the ClpX nucleotide dependent conformational cycle. The transition from Conformation A to Conformation B is mediated through nucleotide exchange in the US position (1st to 2nd ring), with ATP hydrolysis and phosphate release in the ATP* position restoring the A conformation from the B state (2nd to 3rd ring) so that the cycle can repeat. In the new Conformation A (3rd ring), protomer X6 (yellow) adopts the US conformation and the X1 protomer (previous US) moves to the top of the spiral. In this way each protomer of the complex cycles through all positions as ATP is hydrolyzes in successively new ATP* protomer states, requiring the hydrolysis of seven ATPs. (B) Hand-over-hand mechanism of pore-loop mediated translocation. In the first A to B transition depicted in (A) X1 (US protomer) reengages at the top of the spiral and the LS pore 1 loop (X6 in Conformation B) disengages from the bottom of the spiral. As this is repeated the pore loops move "up" the substrate and pull it into the degradation chamber. (C) IGF loop movements accompanying the hand-over-hand movements of ClpX. Shown in the small circles are the seven IGF loop binding sites in ClpP with a '+' sign indicating engagement with an IGF loop of a given ClpX protomer. The binding sites are color coded according to the color of the protomer that interacts with the corresponding site. In conformation A, the IGF loop of X6 is unbound or only weakly bound, while in Conformation B it is bound. A new Conformation A is generated when the IGF loop from the ATP* protomer unbinds. It subsequently reengages with ClpP in a new Conformation B (third and fourth rings in Figure 5A). In this way the IGF loops "step" around the ClpP ring, with each complete rotation requiring the hydrolysis of seven ATPs. (D) Schematic of the ClpX-ClpP interactions during seven ATP hydrolysis steps that lead to a net rotation of ClpX protomers by 60°. Because of the six- to seven-fold symmetry mismatch a total of forty-two ATPs must be hydrolyzed to return the protomers back to their original starting positions in the cycle (*i.e.*, ring 1). Each of the seven ring structures corresponds to Conformation A, with the red arrows indicating the subsequent step of the IGF loop of the ATP* protomer along the cycle. The US protomer in each step is highlighted by the dashed trace.

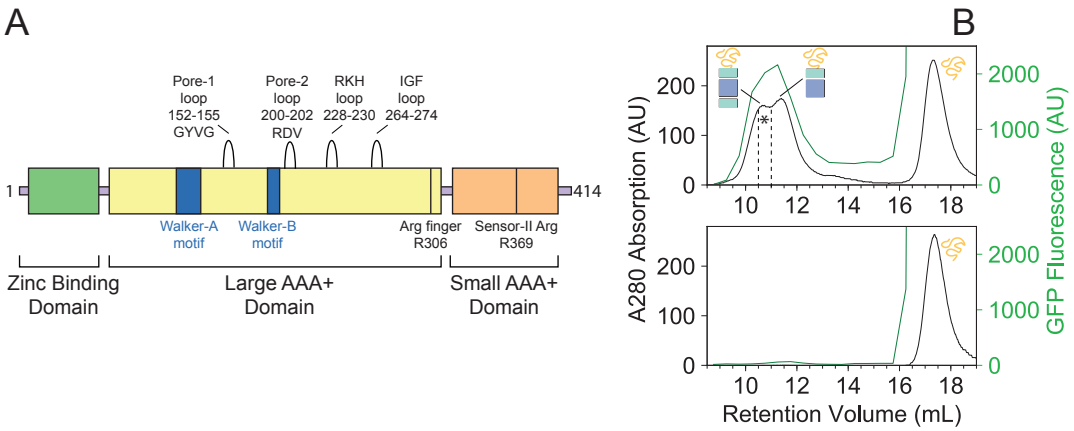

Figure 1 - Figure Supplement 1. (A) NmClpX primary sequence domain map. Important structural and functional motifs are denoted. (B) NmClpXP binds a SsrA-tagged GFP. SEC profiles for ClpXP incubated with GFP-SsrA (top panel) and GFP-SsrA alone (bottom panel) measured using absorbance at 280 nm (black trace) and GFP fluorescence (green trace - λ_{ex}:480nm, λ_{em}:508 nm). The region used for SDS PAGE analysis is highlighted by * (Figure 1C).

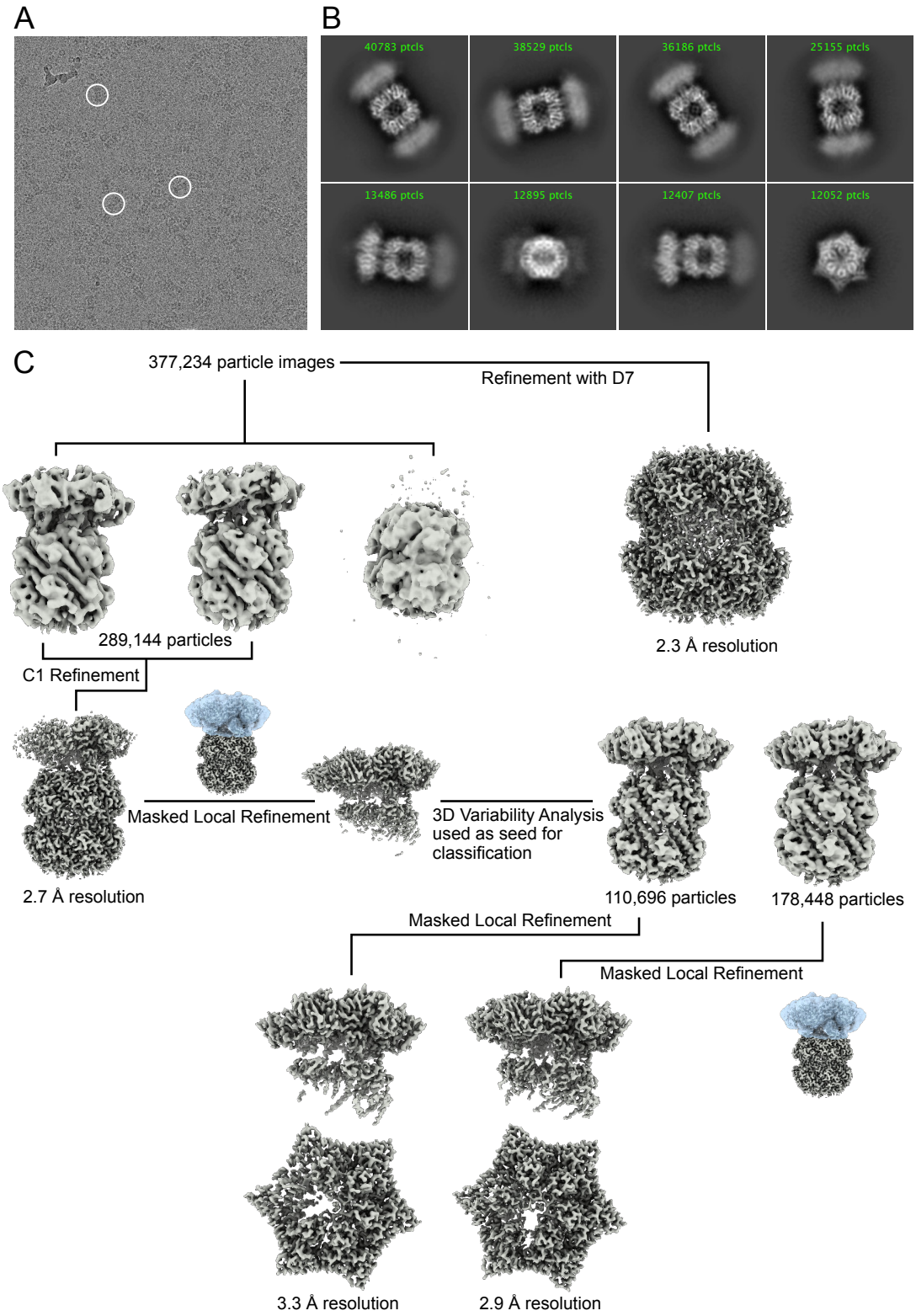

Figure 1 – Figure Supplement 2. Cryo-EM image processing. (A) Representative cryo-EM micrograph of NmClpXP bound to GFP-SsrA. Example complexes are circled in white. (B) Representative 2D class averages of NmClpXP with GFP-SsrA. (C) Image processing workflow used to obtain final maps.

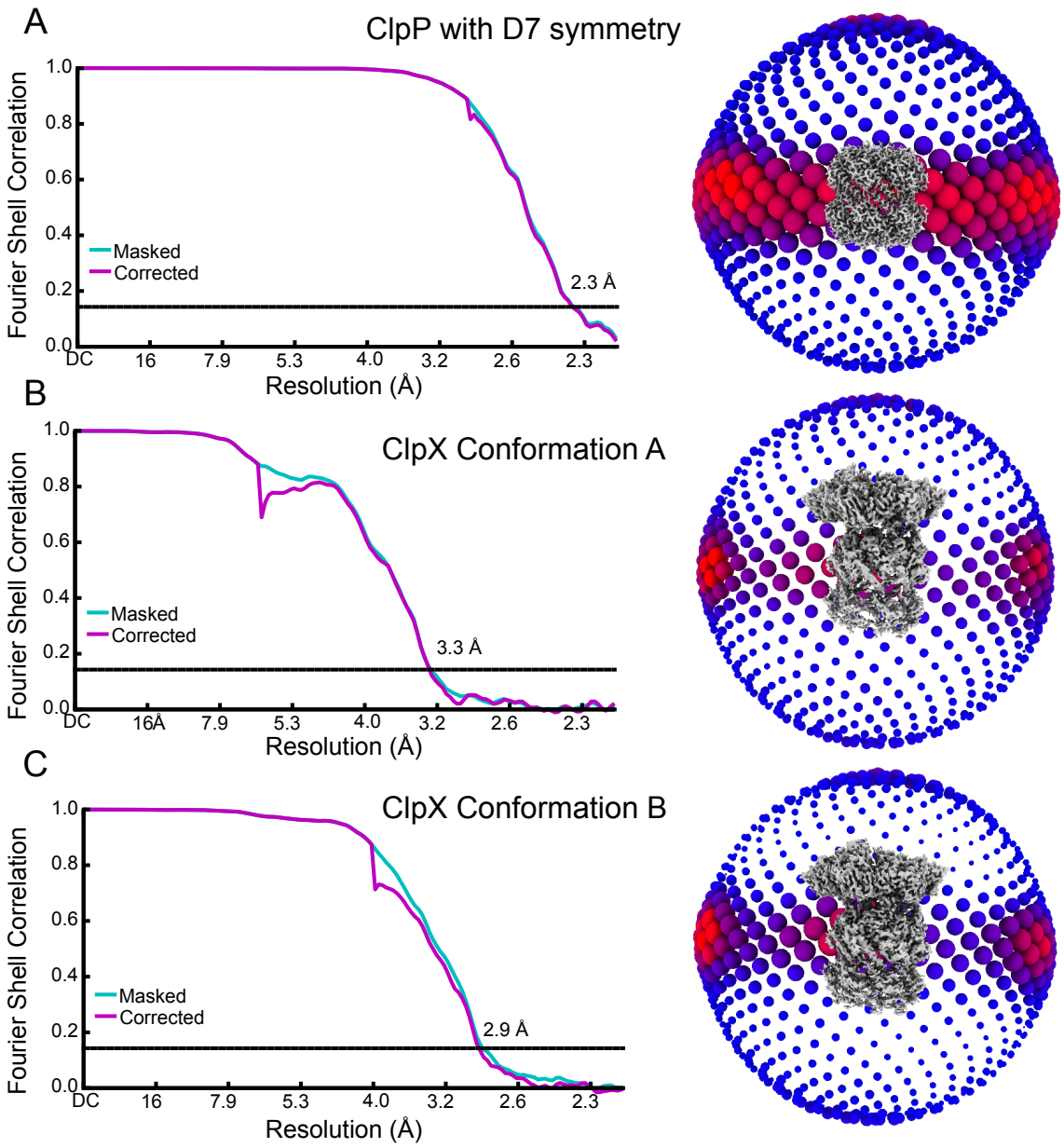

Figure 1 – Figure Supplement 3. Cryo-EM map validation. (A to C) Fourier Shell Correlation (FSC) plots (left) and orientation distribution (right). Resolution values reported are for FSC=0.143.

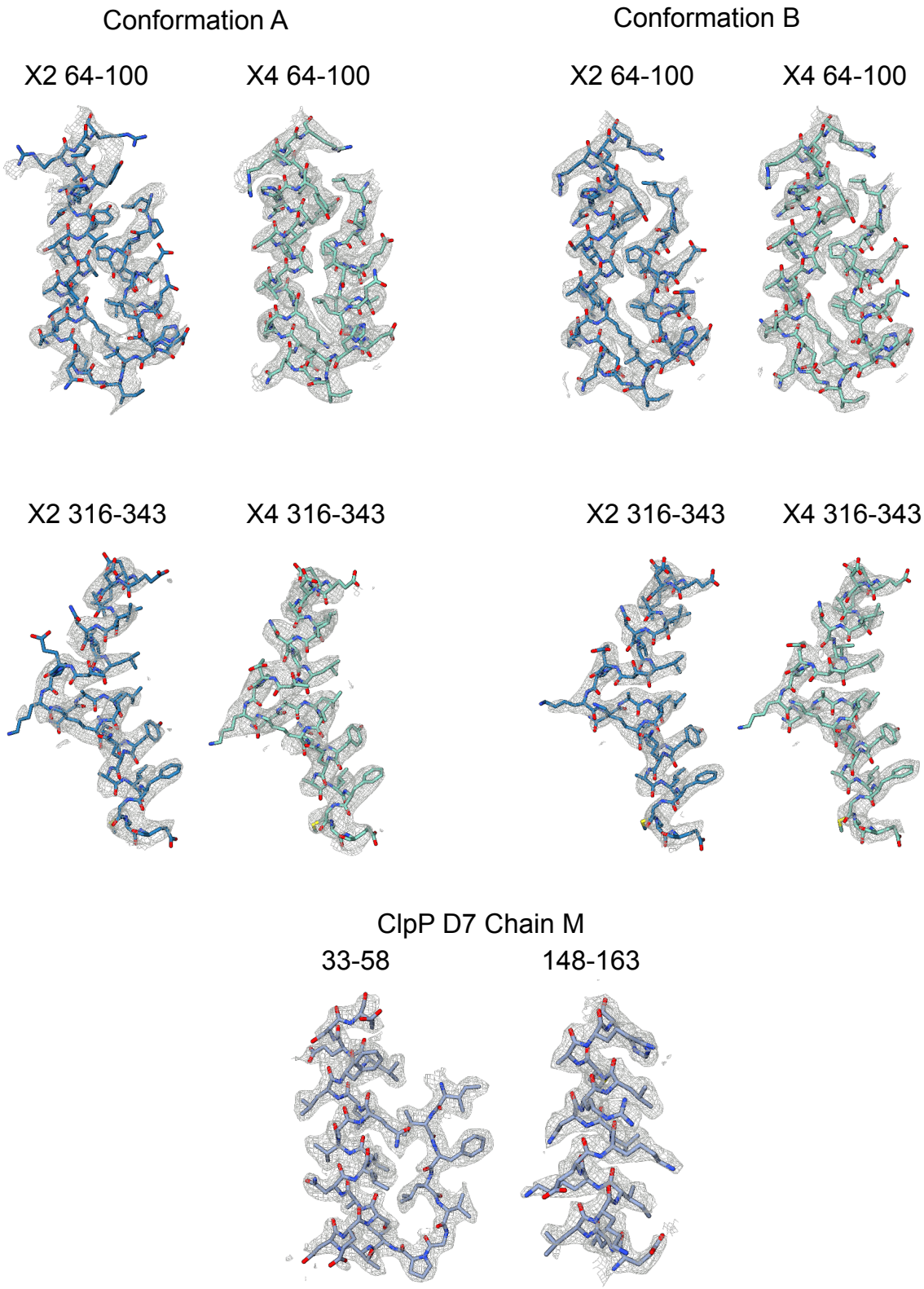

Figure 1 – Figure Supplement 4. Examples of regions of the atomic models built into the experimental cryo-EM maps.

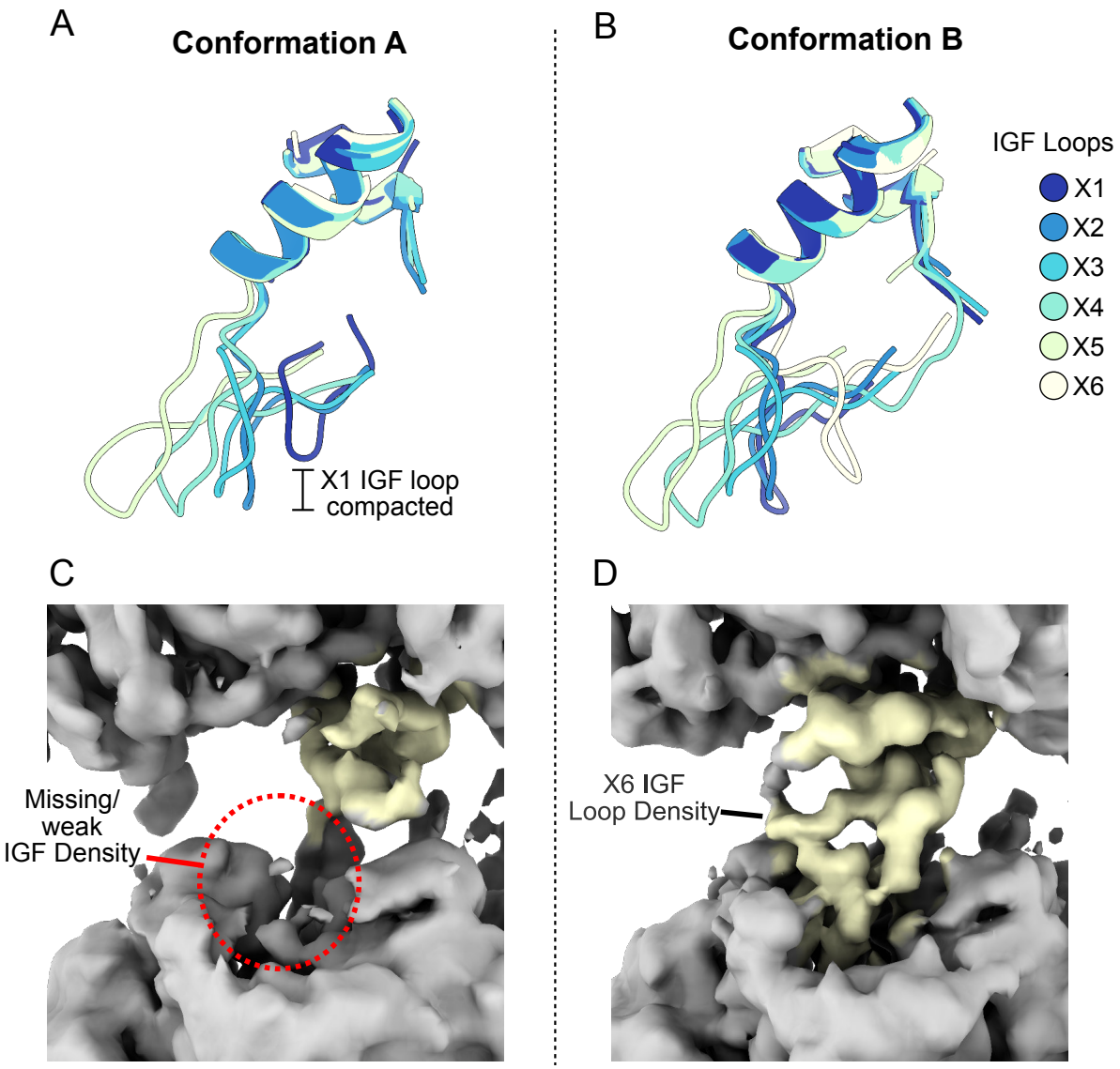

Figure 2 - Figure Supplement 1. IGF loop flexibility. (A and B) Large domains of ClpX were aligned and models for the IGF loops are shown. (C and D) Unsharpened density map for Conformations A and B looking at protomer X6.

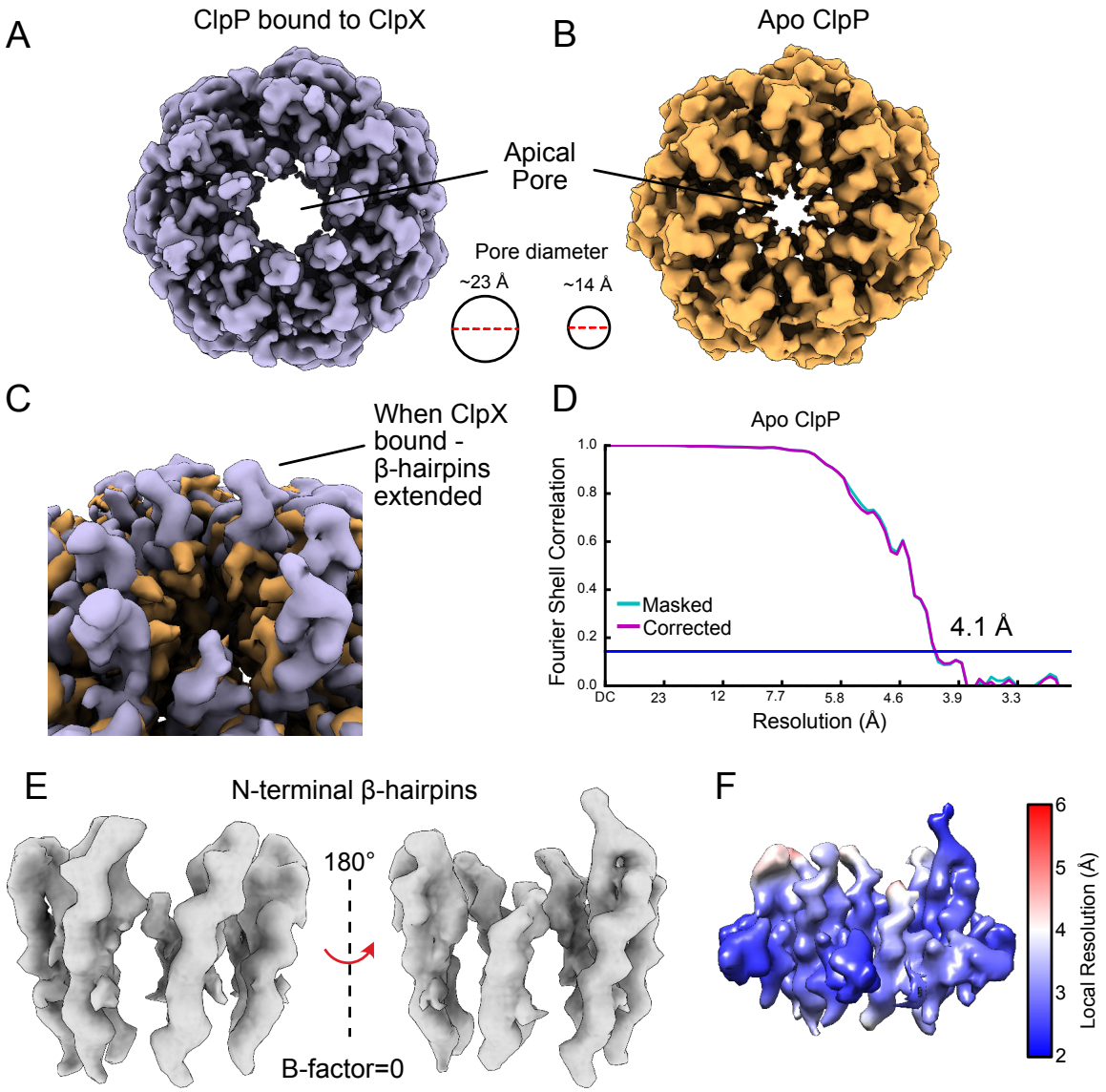

Figure 2 - Figure Supplement 2. The ClpP apical loops extend upwards from the ring surface. (A) Unsharpened density map of the ClpP N-terminal β-hairpins when bound to ClpX. (B) Cryo-EM map of apo ClpP from *N. meningitidis* showing that the apical loops no longer extend "up". (C) ClpX-bound and apo forms of ClpP overlaid. There is no noticeable density for the turn of the ClpP N-terminal β-hairpin in the apo form, and the β-hairpins point inwards, constricting the axial pore of ClpP. (D) Fourier Shell Correlation (FSC) plot for Apo-NmClpP. (E) Closeup view of the N-terminal β-hairpins when bound to ClpX. (F) Density map of the β-hairpins in the ClpXP complex, colored by local resolution.

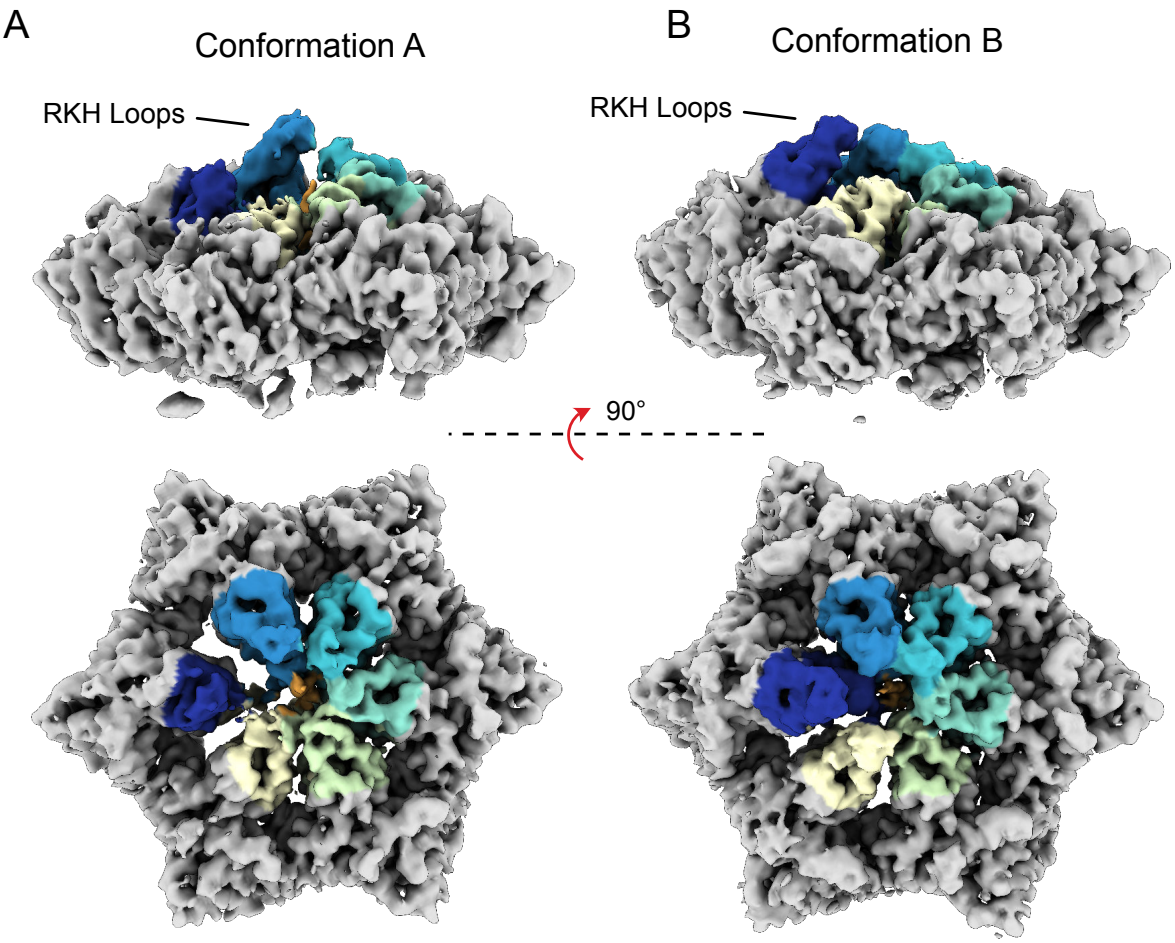

Figure 3 - Figure Supplement 1. RKH loop positions. (A and B) Unsharpened maps for both conformations A and B of ClpX are shown, with RKH loops highlighted in color (coloring done by a radius of 10 Å around residues 220-240).

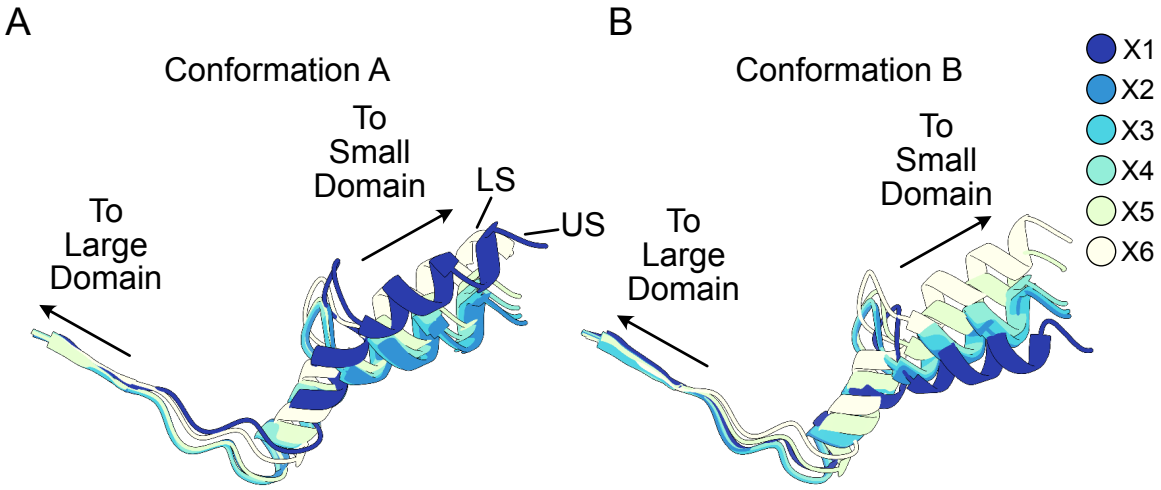

Figure 4 - Figure Supplement 1. Relative orientation between large and small domains of ClpX. (A and B). Residues 308-343 are shown. Note that protomers X1 and X6 in Conformations A and B, respectively, are displaced from substrate. These show among the largest differences in domain orientations.

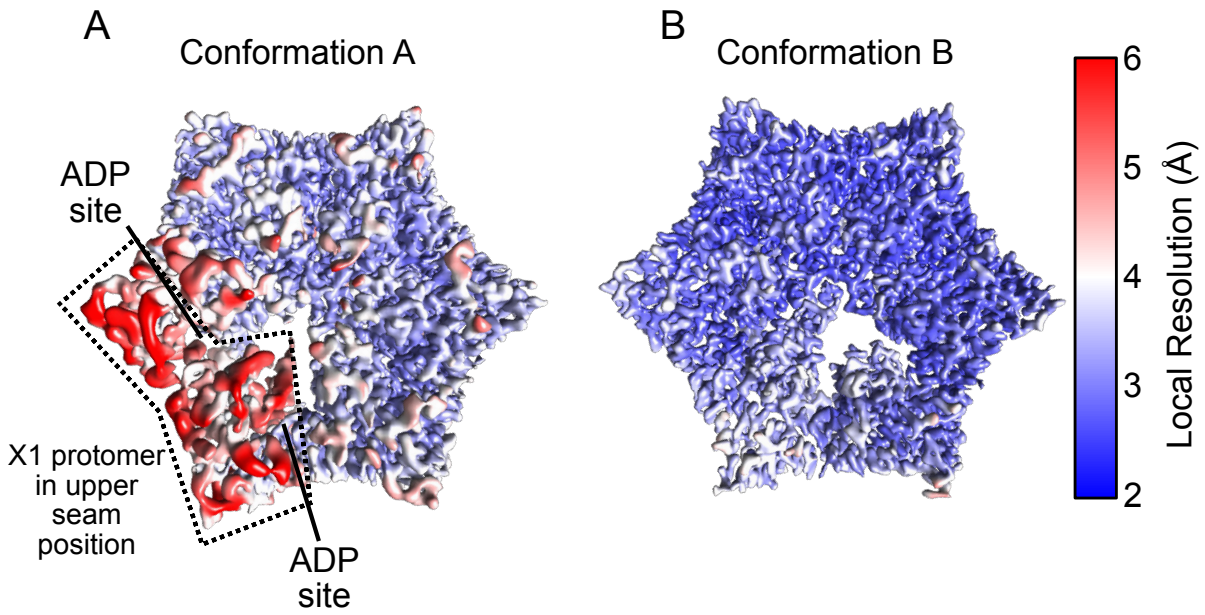

Figure 4 - Figure Supplement 2. Local resolution maps of ClpX. (A and B) Density maps colored by local resolution for Conformations A and B. In Conformation A the US protomer is highlighted with a dashed line.

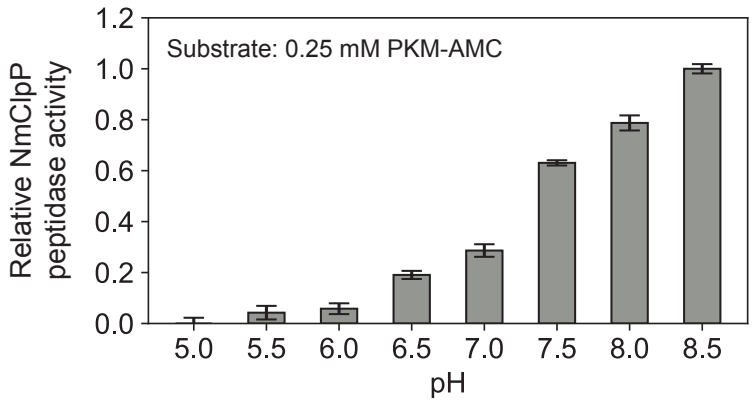

Appendix Figure 1. Peptidase rate measurements of NmClpP as a function of pH, monitored using the fluorogenic substrate PKM-AMC.

Video 1. Overview of the substrate bound ClpXP complex (Conformation B).

Video 2. Hand-over-hand translocation cycle of the ClpXP complex. Interpolation between states A → B → A → B. Side and top views of the complex are shown (top), along with the pore-1 loop Tyr153 and substrate (bottom left) as well as IGF loops (bottom right).

Video 3. ClpX precession on the ClpP apical surface. Repeated interpolation between states reveals a precession of the ClpX ring as its IGF loops are placed successively in different ClpP binding sites. The position of the empty binding pocket on ClpP undergoes a complete cycle around the complex for every 60° rotation of the ClpX ring relative to the ClpP ring.

Supplementary File 1. Cryo-EM data acquisition, processing, model statistics, and data deposition. (A) CryoEM data acquisition and image processing. (B) Map and Model statistics. (C) Residues excluded in atomic models. (D) Deposited maps and associated coordinate files.

Materials and Methods:

Plasmids and constructs Codon-optimized genes encoding NmClpX (Uniprot entry: Q9JYY3) bearing an N-terminal His_6-TEV affinity tag and ClpP (Uniprot entry: Q9JZ38) with an N-terminal His_6-SUMO tag were synthesized by GenScript (Piscataway, NJ, USA) and cloned into the NdeI and BamHI sites of pET28a+ (Novagen, Madison, WI, USA). Point mutations were introduced with the Quikchange mutagenesis method (Agilent, Santa Clara, CA, USA).

Expression and purification of NmClpP and NmClpX Transformed Codon+ *E. coli* BL21(DE3) cells were grown in LB media at 37 °C. Protein over-expression was induced by addition of 0.2 mM IPTG at OD_{600}=1.0 and was allowed to proceed overnight at 18 °C. Cells were lysed in buffer containing 50 mM Tris, 300 KCl, 10 mM imidazole, 10% glycerol, pH 7.0 and NmClpP

and NmClpX proteins purified by Ni-affinity chromatography [HisTrap HP (GE)] in lysis buffer. Bound proteins were eluted from the Ni column by increasing the imidazole concentration to 500 mM. The affinity tag was removed by the addition of TEV (for ClpX) or Ulp1 (for ClpP) protease followed by dialysis against lysis/wash buffer that included 5 mM DTT. Following a reverse Ni-affinity chromatography step, the flow-through, free from the cleaved tag and other impurities, was concentrated with an Amicon Ultra-15 50K MWCO (Millipore) concentrator and subjected to size exclusion chromatography (SEC) with a Superdex 200 Increase 10/300 (GE) column in SEC buffer (50 mM imidazole, 100 mM KCl, 5 mM DTT, pH 7.0). Fractions corresponding to NmClpX and NmClpP were pooled and stored at 4 °C in the SEC buffer until further use. Salts containing magnesium were avoided during the purification of NmClpX to prevent protein aggregation. Protein concentrations were determined in 8 M GdnCl using extinction coefficient values (7450 M^{-1} cm^{-1} for ClpP, 8940 M^{-1} cm^{-1} for ClpX) determined with ExPASy's ProtParam (69).

Expression and purification of GFP-SsrA. Green fluorescent protein (GFP) bearing an 11-residue SsrA degradation tag at its carboxyl terminus and a non-cleavable N-terminal His×6 tag was purified by Ni affinity chromatography followed by SEC on a HiLoad 16/60 Superdex 75 pg column (GE).

Peptidase rate measurements of NmClpP as a function of pH. The peptidase activity of NmClpP was measured at 37 ºC with Acetyl-L-Pro-L-Lys-L-Met bearing a C-terminal fluorogenic 7-amino-4-methylcoumarin group (PKM-AMC) as substrate. The reaction was followed with a Synergy Neo2 96-well microplate reader making a measurement every 21 seconds for 60 minutes at λ_{ex}: 355 nm, λ_{em}: 460 nm. Each well contained 1 µM NmClpP (monomer concentration), 250 µM PKM-AMC, 50 mM citrate, 50 mM phosphate, 50 mM Tris,

555 100 mM KCl in a total volume of 100 µL adjusted to the appropriate pH. Activities are derived
556 from initial rates extracted and analyzed using a python script written in-house. Standard errors
557 are calculated from repeating each reaction in triplicate.

558 ***GFP-SsrA degradation assays.*** Degradation of 1 µM samples of GFP-SsrA was followed by the
559 loss of GFP fluorescence (λ_{ex}: 480 nm, λ_{em}: 508 nm) with a Synergy Neo2 96-well microplate
560 reader at 25 °C. The wells included an ATP-regeneration system (70) that contained 1.5 mM
561 phosphoenolpyruvate, 0.2 mM NADH, 40 µg/mL pyruvate kinase, 40 µg/mL lactate
562 dehydrogenase, and 2 mM MgATP at pH 8.2. In some assays solutions also contained WT
563 NmClpX at 0.5 µM concentration (hexamer) and/or WT ClpP at a 0.25 µM concentration
564 (tetradecamer), as indicated in Figure 1B. All assays were performed in triplicate.

565 ***Preparation of samples for cryo-EM.*** A 1 mL mixture containing 10 µM (tetradecamer)
566 NmClpP and 20 µM NmClpX together with 200 µM GFP-SsrA was incubated with 20 mM
567 MgATP for 10 minutes at room temperature. This mixture was applied to a Superdex 200
568 Increase 10/300 (GE) column equilibrated with 50 mM bicine, 100 mM KCl, 2 mM MgATP, pH
569 adjusted to 8.2 at room temperature (equivalent to pH 8.5 at 4 °C – see Appendix Figure 1), as
570 the running buffer. Following SEC, a 0.5 mL fraction (denoted with a * in Figure 1 – Figure
571 Supplement 1) containing doubly capped ClpXP bound to GFP-SsrA was supplemented with 20
572 µM GFP-SsrA and vitrified immediately without the addition of any cross-linking agent or
573 detergent.

574 ***Sample vitrification.*** 2.5 µL of the sample mixtures were applied to nanofabricated holey gold
575 grids (71–73) with a hole size of ~1 µm, that had been glow discharged in air for 15 seconds.
576 Grids were blotted on both sides using a FEI Vitrobot mark III for 15 seconds at 4 °C and ~100%
577 relative humidity before freezing in a liquid ethane/propane mixture (74).

578 ***Electron Microscopy:*** NmClpXP was imaged with a Thermo Fisher Scientific Titan Krios G3
579 microscope operating at 300 kV and equipped with a FEI Falcon III DDD camera. Structures
580 were calculated from counting mode movies consisting of 30 frames, obtained over a 60 second
581 exposure with defocuses ranging from 0.9 to 1.7 μm. Movies were at a nominal magnification of
582 75000× corresponding to a calibrated pixel size of 1.06 Å and with an exposure of 0.8
583 electrons/pixel/s, giving a total exposure of 43 electrons/Å^2. 2680 movies were collected using
584 the microscope's *EPU* software. The Apo-NmClpP structure (with no ClpX or GFP present) was
585 calculated from data obtained using a FEI Tecnai F20 electron microscope operating at 200 kV
586 and equipped with a Gatan K2 Summit direct detector device camera. Movies consisting of 30
587 frames over a 15 second exposure were obtained with defocuses ranging from 1.7 to 2.9 μm.
588 Movies were collected in counting mode at a nominal magnification of 25000× corresponding to
589 a calibrated pixel size of 1.45 Å and with an exposure of 5 electrons/pixel/s, and a total exposure
590 of 35 electrons/Å^2. 122 movies were collected using Digital Micrograph software.
591 ***EM image analysis:*** Patch based whole frame alignment and exposure weighting was performed
592 in *cryoSPARC* v2 (55) with a 10×10 grid and the resulting averages of frames were used for
593 patch based contrast transfer function (CTF) determination. Templates for particle selection were
594 generated by 2D classification of manually selected particles. Particle images were extracted in
595 300×300-pixel boxes for further analysis. *Ab inito* map calculation was performed on a random
596 subset of 30,000 particle images, generating an initial map showing density for the complex of a
597 ClpP tetradecamer bound to two ClpX hexamers. A single round of 2D classification was used to
598 remove images of damaged particles and other contaminants from a dataset of 466,549 particle
599 images, with selected classes leaving 377,234 particle images for further analysis. Homogeneous

refinement of these particle images using D7 symmetry yielded a map of the complex, with good density for only the ClpP portion, at 2.3 Å resolution.

To improve the density of the ClpX portion of the map, a round of *Ab initio* classification was performed using three classes, of which two classes containing 289,144 particle images had good density for ClpX, with the remaining class containing mostly density for ClpP. Refinement of these particle images with C1 symmetry resulted in a map of the ClpXP complex at a nominal resolution of 2.8 Å, but with poorly defined density for much of ClpX. To improve the interpretability of the map in the ClpX region, local refinement was performed with a mask around the six ClpX subunits without performing signal subtraction for ClpP. This refinement greatly improved the map in the ClpX region, while blurring the density at the distal ClpP ring (indicative of flexibility between ClpX and ClpP). However, density for two of the ClpX subunits remained fragmented and at lower resolution. To help resolve the heterogeneity of this region "3D variability analysis" was performed, which utilizes principle component analysis to separate conformations. Clustering was performed along three eigenvectors. Two clusters were identified along a single eigenvector corresponding to two conformations of ClpX bound to substrate. From the trajectory identified, the two endpoints were used to seed a heterogeneous classification in which the O-EM learning rate was reduced 10-fold to preserve the original character of the seeds yielding two classes split ~ 40%:60% with 110,696 and 178,448 particle images for Conformations A and B respectively. Subsequent non-uniform refinement yielded maps at 3.3 Å and 2.9 Å respectively, which were then used for model building.

For Apo-NmClpP the same preprocessing steps were applied as described above, and 100,132 particle images were extracted in 160×160-pixel boxes for further analysis. Rounds of

622 2D classification and *ab initio* classification led to a subset of 50,400 particle images that were
623 used to refined a map to 4.1 Å resolution.

624 ***Atomic Model Building and Refinement:*** To model NmClpP, the crystal structure of NmClpP
625 (PDBID: 5DKP) (56) was rigidly fit with UCSF Chimera (75) into the 2.3 Å D7 symmetric map,
626 followed by relaxation with Rosetta using the density map as an additional term in the scoring
627 function (76), and utilizing D7 non crystallographic symmetry. The best scoring model was then
628 rigidly fit into the C1 symmetry focussed maps for Conformation A and B. Visual inspection and
629 real space refinement in *Coot* (77) was then used to better fit the model into the density where it
630 deviated from the ideal symmetry version, specifically in areas where ClpX contacted ClpP, and
631 the apical loops (N-terminal β-hairpins).

632 For NmClpX, Phyre2 (78) was used to perform one-to-one threading onto the previous
633 crystal structure of ClpX from *E. coli* (PDBID 3HWS chain A) (48). A single chain was then
634 rigidly docked into the X3 position of the 2.9 Å map, and real space refinement and *Ab initio*
635 model building of regions that poorly fit the density, as well as for regions missing from the
636 homology model was performed in *Coot* (77). This model was then relaxed with Rosetta (76),
637 and rigidly fit into the density for the other five ClpX protomers. Iterative rounds of real space
638 refinement and *Ab initio* model building in *Coot* (77), relaxation in Rosetta (76), and real space
639 refinement in Phenix (79), were then used to create the final model. To model Conformation A,
640 the model for Conformation B was used as a starting point before iterative rounds of real space
641 refinement and *Ab initio* model building in *Coot*, relaxation in Rosetta, and real space refinement
642 in Phenix. Models were evaluated with Molprobity (80) and EMRinger (81). Figures and movies
643 were generated in UCSF Chimera (75) and UCSF ChimeraX (82), and colors chosen with
644 ColorBrewer (83).

Acknowledgements

We thank Dr. Samir Benlekbir for cryo-EM data collection on the Titan Krios. ZAR and SV were supported by a scholarship and a postdoctoral fellowship from the Canadian Institutes of Health Research, respectively. LEK and JLR were supported by the Canada Research Chairs program. This research was funded by Canadian Institutes of Health Research grants MOP-133408 (LEK), PJT-162186 (JLR), and PJT-148564 (WAH). Titan Krios cryo-EM data were collected at the Toronto High-Resolution High-Throughput cryo-EM facility supported by the Canadian Foundation for Innovation and Ontario Research Fund.

References:

1. A. O. Olivares, T. A. Baker, R. T. Sauer, Mechanistic insights into bacterial AAA+ proteases and protein-remodelling machines. *Nat. Rev. Microbiol.* **14**, 33–44 (2016).

2. A. L. Goldberg, Protein degradation and protection against misfolded or damaged proteins. *Nature* **426**, 895–899 (2003).

3. D. Frees, U. Gerth, H. Ingmer, Clp chaperones and proteases are central in stress survival, virulence and antibiotic resistance of Staphylococcus aureus. *Int. J. Med. Microbiol.* **304**, 142–149 (2014).

4. C. M. Pickart, R. E. Cohen, Proteasomes and their kin: proteases in the machine age. *Nat. Rev. Mol. Cell Biol.* **5**, 177–187 (2004).

5. V. Bhandari, K. S. Wong, J. L. Zhou, M. F. Mabanglo, R. A. Batey, W. A. Houry, The Role of ClpP Protease in Bacterial Pathogenesis and Human Diseases. *ACS Chem. Biol.* **13**, 1413–1425 (2018).

6. T. A. Baker, R. T. Sauer, ClpXP, an ATP-powered unfolding and protein-degradation machine. *Biochim. Biophys. Acta* **1823**, 15–28 (2012).

7. T. Böttcher, S. A. Sieber, β-Lactones as Privileged Structures for the Active-Site Labeling of Versatile Bacterial Enzyme Classes. *Angew. Chem. Int. Ed.* **47**, 4600–4603 (2008).

8. M. W. Hackl, M. Lakemeyer, M. Dahmen, M. Glaser, A. Pahl, K. Lorenz-Baath, T. Menzel, S. Sievers, T. Böttcher, I. Antes, H. Waldmann, S. A. Sieber, Phenyl Esters Are Potent Inhibitors of Caseinolytic Protease P and Reveal a Stereogenic Switch for Deoligomerization. *J. Am. Chem. Soc.* **137**, 8475–8483 (2015).

9. M. Lakemeyer, E. Bertosin, F. Möller, D. Balogh, R. Strasser, H. Dietz, S. A. Sieber, Tailored peptide phenyl esters block ClpXP proteolysis by an unusual breakdown into a

heptamer-hexamer assembly. *Angew. Chemie Int. Ed.* **0** (2019).

10. W. Gao, *et al.*, The Cyclic Peptide Ecumicin Targeting ClpC1 Is Active againstMycobacterium tuberculosis In Vivo. *Antimicrob. Agents Chemother.* **59**, 880 (2015).

11. E. Gavrish, *et al.*, Lassomycin, a Ribosomally Synthesized Cyclic Peptide, Kills Mycobacterium tuberculosis by Targeting the ATP-Dependent Protease ClpC1P1P2. *Chem. Biol.* **21**, 509–518 (2014).

12. M. P. Choules, *et al.*, Rufomycin Targets ClpC1 Proteolysis in Mycobacterium tuberculosis and M. abscessus. *Antimicrob. Agents Chemother.* **63**, e02204-18 (2019).

13. C. Fetzer, V. S. Korotkov, R. Thänert, K. M. Lee, M. Neuenschwander, J. P. von Kries, E. Medina, S. A. Sieber, A Chemical Disruptor of the ClpX Chaperone Complex Attenuates the Virulence of Multidrug-Resistant Staphylococcus aureus. *Angew. Chemie Int. Ed.* **56**, 15746–15750 (2017).

14. J. Kirstein, A. Hoffmann, H. Lilie, R. Schmidt, H. Rübsamen-Waigmann, H. Brötz-Oesterhelt, A. Mogk, K. Turgay, The antibiotic ADEP reprogrammes ClpP, switching it from a regulated to an uncontrolled protease. *EMBO Mol. Med.* **1**, 37–49 (2009).

15. M. Gersch, K. Famulla, M. Dahmen, C. Göbl, I. Malik, K. Richter, V. S. Korotkov, P. Sass, H. Rübsamen-Schaeff, T. Madl, H. Brötz-Oesterhelt, S. A. Sieber, AAA+ chaperones and acyldepsipeptides activate the ClpP protease via conformational control. *Nat. Commun.* **6**, 6320 (2015).

16. K. S. Wong, *et al.*, Acyldepsipeptide Analogs Dysregulate Human Mitochondrial ClpP Protease Activity and Cause Apoptotic Cell Death. *Cell Chem. Biol.* **25**, 1017–1030.e9 (2018).

17. E. Culp, G. D. Wright, Bacterial proteases, untapped antimicrobial drug targets. *J. Antibiot. (Tokyo).* **70**, 366–377 (2017).

18. I. T. Malik, H. Brotz-Oesterhelt, Conformational control of the bacterial Clp protease by natural product antibiotics. *Nat. Prod. Rep* **34**, 815–831 (2017).

19. R. M. Raju, A. L. Goldberg, E. J. Rubin, Bacterial proteolytic complexes as therapeutic targets. *Nat. Rev. Drug Discov.* **11**, 777–789 (2012).

20. C. A. Goard, A. D. Schimmer, Mitochondrial matrix proteases as novel therapeutic targets in malignancy. *Oncogene* **33**, 2690 (2013).

21. K. S. Wong, W. A. Houry, "Recent Advances in Targeting Human Mitochondrial AAA+ Proteases to Develop Novel Cancer Therapeutics" in *Mitochondria in Health and in Sickness*, A. Urbani, M. Babu, Eds. (Springer Singapore, 2019), pp. 119–142.

22. J. Wang, J. A. Hartling, J. M. Flanagan, The Structure of ClpP at 2.3 A° Resolution Suggests a Model for ATP-Dependent Proteolysis. *Cell* **91**, 447–456 (1997).

23. K. Liu, A. Ologbenla, W. A. Houry, Dynamics of the ClpP serine protease: A model for self-compartmentalized proteases. *Crit. Rev. Biochem. Mol. Biol.* **49**, 400–412 (2014).

24. F. Förster, P. Unverdorben, P. Śledź, W. Baumeister, Unveiling the Long-Held Secrets of the 26S Proteasome. *Structure* **21**, 1551–1562 (2013).

25. E. Kish-Trier, C. P. Hill, Structural Biology of the Proteasome. *Annu. Rev. Biophys.* **42**, 29–49 (2013).

26. J. Ortega, H. S. Lee, M. R. Maurizi, A. C. Steven, Alternating translocation of protein substrates from both ends of ClpXP protease. *EMBO J.* **21**, 4938–4949 (2002).

27. J. Ortega, S. K. Singh, T. Ishikawa, M. R. Maurizi, A. C. Steven, Visualization of Substrate Binding and Translocation by the ATP-Dependent Protease, ClpXP. *Mol. Cell* **6**,

722 1515–1521 (2000).

723 28. M. Kessel, M. R. Maurizi, B. Kim, E. Kocsis, B. L. Trus, S. K. Singh, A. C. Steven,
724 Homology in Structural Organization Between E. coli ClpAP Protease and the Eukaryotic
725 26 S Proteasome. *J. Mol. Biol.* **250**, 587–594 (1995).

726 29. M. E. Lee, T. A. Baker, R. T. Sauer, Control of Substrate Gating and Translocation into
727 ClpP by Channel Residues and ClpX Binding. *J. Mol. Biol.* **399**, 707–718 (2010).

728 30. D. H. S. Li, Y. S. Chung, M. Gloyd, E. Joseph, R. Ghirlando, G. D. Wright, Y. Q. Cheng,
729 M. R. Maurizi, A. Guarne, J. Ortega, Acyldepsipeptide Antibiotics Induce the Formation
730 of a Structured Axial Channel in ClpP: A Model for the ClpX/ClpA-Bound State of ClpP.
731 *Chem. Biol.* **17**, 959–969 (2010).

732 31. G. Effantin, M. R. Maurizi, A. C. Steven, Binding of the ClpA Unfoldase Opens the Axial
733 Gate of ClpP Peptidase. *J. Biol. Chem.* **285**, 14834–14840 (2010).

734 32. Y.-I. Kim, I. Levchenko, K. Fraczkowska, R. V Woodruff, R. T. Sauer, T. A. Baker,
735 Molecular determinants of complex formation between Clp/Hsp100 ATPases and the
736 ClpP peptidase. *Nat. Struct. Biol.* **8**, 230–233 (2001).

737 33. S. A. Joshi, G. L. Hersch, T. A. Baker, R. T. Sauer, Communication between ClpX and
738 ClpP during substrate processing and degradation. *Nat Struct Mol Biol* **11**, 404–411
739 (2004).

740 34. A. J. Amor, K. R. Schmitz, T. A. Baker, R. T. Sauer, Roles of the ClpX IGF loops in ClpP
741 association, dissociation, and protein degradation. *Protein Sci.* **28**, 756–765 (2019).

742 35. A. Gribun, M. S. Kimber, R. Ching, R. Sprangers, K. M. Fiebig, W. A. Houry, The ClpP
743 Double Ring Tetradecameric Protease Exhibits Plastic Ring-Ring Interactions, and the N
744 Termini of Its Subunits Form Flexible Loops That Are Essential for ClpXP and ClpAP

Complex Formation. *J. Bio. Chem.* **280**, 16185–16196 (2005).

36. L. D. Jennings, J. Bohon, M. R. Chance, S. Licht, The ClpP N-Terminus Coordinates Substrate Access with Protease Active Site Reactivity. *Biochemistry* **47**, 11031–11040 (2008).

37. A. Martin, T. A. Baker, R. T. Sauer, Diverse Pore Loops of the AAA+ ClpX Machine Mediate Unassisted and Adaptor-Dependent Recognition of ssrA-Tagged Substrates. *Mol. Cell* **29**, 441–450 (2008).

38. A. Martin, T. A. Baker, R. T. Sauer, Pore loops of the AAA+ ClpX machine grip substrates to drive translocation and unfolding. *Nat Struct Mol Biol* **15**, 1147–1151 (2008).

39. N. Monroe, H. Han, P. S. Shen, W. I. Sundquist, C. P. Hill, Structural basis of protein translocation by the Vps4-Vta1 AAA ATPase. *Elife* **6** (2017).

40. H. Yu, T. J. Lupoli, A. Kovach, X. Meng, G. Zhao, C. F. Nathan, H. Li, ATP hydrolysis-coupled peptide translocation mechanism of Mycobacterium tuberculosis ClpB. *Proc. Natl. Acad. Sci. U. S. A.* **115**, E9560–E9569 (2018).

41. A. H. De la Peña, E. A. Goodall, S. N. Gates, G. C. Lander, A. Martin, Substrate-engaged 26S proteasome structures reveal mechanisms for ATP-hydrolysis–driven translocation. *Science (80-.).* **362**, eaav0725 (2018).

42. M. Shin, A. Asmita, C. Puchades, E. Adjei, R. L. Wiseman, A. W. Karzai, G. C. Lander, Distinct Structural Features of the Lon Protease Drive Conserved Hand-over-Hand Substrate Translocation. *bioRxiv*, 617159 (2019).

43. Z. A. Ripstein, R. Huang, R. Augustyniak, L. E. Kay, J. L. Rubinstein, Structure of a AAA+ unfoldase in the process of unfolding substrate. *Elife* **6**, e25754 (2017).

44. S. N. Gates, *et al.*, Ratchet-like polypeptide translocation mechanism of the AAA +

768 disaggregase Hsp104. **1052**, 1–13 (2017).

769 45. M. Li, O. Kandror, T. Akopian, P. Dharkar, A. Wlodawer, M. R. Maurizi, A. L. Goldberg,
770 Structure and Functional Properties of the Active Form of the Proteolytic Complex,
771 ClpP1P2, from Mycobacterium tuberculosis. *J. Biol. Chem.* **291**, 7465–7476 (2016).

772 46. S. R. Geiger, T. Bottcher, S. A. Sieber, P. Cramer, A Conformational Switch Underlies
773 ClpP Protease Function. *Angew. Chem. Int. Ed.* **50**, 5749–5752 (2011).

774 47. J. Ishizawa, *et al.*, Mitochondrial ClpP-Mediated Proteolysis Induces Selective Cancer
775 Cell Lethality. *Cancer Cell* (2019)
776 https:/doi.org/https://doi.org/10.1016/j.ccell.2019.03.014.

777 48. S. E. Glynn, A. Martin, A. R. Nager, T. A. Baker, R. T. Sauer, Structures of Asymmetric
778 ClpX Hexamers Reveal Nucleotide-Dependent Motions in a AAA+ Protein-Unfolding
779 Machine. *Cell* **139**, 744–756 (2007).

780 49. M. C. Bewley, V. Graziano, K. Griffin, J. M. Flanagan, The asymmetry in the mature
781 amino-terminus of ClpP facilitates a local symmetry match in ClpAP and ClpXP
782 complexes. *J. Struct. Biol.* **153**, 113–128 (2006).

783 50. F. Beuron, M. R. Maurizi, D. M. Belnap, E. Kocsis, F. P. Booy, M. Kessel, A. C. Steven,
784 At Sixes and Sevens: Characterization of the Symmetry Mismatch of the ClpAP
785 Chaperone-Assisted Protease. *J. Mol. Biol.* **123**, 248–259 (1998).

786 51. P. Majumder, T. Rudack, F. Beck, R. Danev, G. Pfeifer, I. Nagy, W. Baumeister, Cryo-
787 EM structures of the archaeal PAN-proteasome reveal an around-the-ring ATPase cycle.
788 *Proc. Natl. Acad. Sci.* **116**, 534 LP-539 (2019).

789 52. G. L. Hersch, R. E. Burton, D. N. Bolon, T. A. Baker, R. T. Sauer, Asymmetric
790 Interactions of ATP with the AAA+ ClpX6 Unfoldase: Allosteric Control of a Protein

Machine. *Cell* **121**, 1017–1027 (2005).

53. R. Grimaud, M. Kessel, F. Beuron, A. C. Steven, M. R. Maurizi, Enzymatic and Structural Similarities between the Escherichia coli ATP-dependent Proteases, ClpXP and ClpAP. *J. Biol. Chem.* **273**, 12476–12481 (1998).

54. J. M. Jones, D. J. Welty, H. Nakai, Versatile Action of Escherichia coli ClpXP as Protease or Molecular Chaperone for Bacteriophage Mu Transposition. *J. Biol. Chem.* **273**, 459–465 (1998).

55. A. Punjani, J. L. Rubinstein, D. J. Fleet, M. A. Brubaker, cryoSPARC: algorithms for rapid unsupervised cryo-EM structure determination. *Nat. Methods* **14**, 290–+ (2017).

56. J. D. Goodreid, J. Janetzko, J. P. Santa Maria, K. S. Wong, E. Leung, B. T. Eger, S. Bryson, E. F. Pai, S. D. Gray-Owen, S. Walker, W. A. Houry, R. A. Batey, Development and Characterization of Potent Cyclic Acyldepsipeptide Analogues with Increased Antimicrobial Activity. *J. Med. Chem.* **59**, 624–646 (2016).

57. A. Martin, T. A. Baker, R. T. Sauer, Distinct static and dynamic interactions control ATPase-Peptidase communication in a AAA plus protease. *Mol. Cell* **27**, 41–52 (2007).

58. J. Ortega, H. S. Lee, M. R. Maurizi, A. C. Steven, ClpA and ClpX ATPases bind simultaneously to opposite ends of ClpP peptidase to form active hybrid complexes. *J. Struct. Biol.* **146**, 217–226 (2004).

59. S. K. Singh, R. Grimaud, J. R. Hoskins, S. Wickner, M. R. Maurizi, Unfolding and internalization of proteins by the ATP-dependent proteases ClpXP and ClpAP. *Proc. Natl. Acad. Sci.* **97**, 8898 LP-8903 (2000).

60. A. Martin, T. A. Baker, R. T. Sauer, Distinct Static and Dynamic Interactions Control ATPase-Peptidase Communication in a AAA+ Protease. *Mol. Cell* **27**, 41–52 (2007).

814 61. C. M. Farrell, T. A. Baker, R. T. Sauer, Altered Specificity of a AAA+ Protease. *Mol. Cell*
815 **25**, 161–166 (2007).
816 62. S. M. Siddiqui, R. T. Sauer, T. A. Baker, Role of the processing pore of the ClpX AAA+
817 ATPase in the recognition and engagement of specific protein substrates. *Genes Dev.* **18**,
818 369–374 (2004).
819 63. R. Augustyniak, L. E. Kay, Cotranslocational processing of the protein substrate
820 calmodulin by an AAA+ unfoldase occurs via unfolding and refolding intermediates.
821 *Proc. Natl. Acad. Sci.* **115**, E4786 LP-E4795 (2018).
822 64. C. Gatsogiannis, D. Balogh, F. Merino, S. A. Sieber, S. Raunser, Cryo-EM structure of the
823 ClpXP protein degradation machinery. *bioRxiv*, 638692 (2019).
824 65. X. Fei, T. A. Bell, S. Jenni, B. M. Stinson, T. A. Baker, S. C. Harrison, R. T. Sauer,
825 Structures of the ATP-fueled ClpXP proteolytic machine bound to protein substrate.
826 *bioRxiv*, 704999 (2019).
827 66. E. J. Enemark, L. Joshua-Tor, Mechanism of DNA translocation in a replicative
828 hexameric helicase. *Nature* **442**, 270–275 (2006).
829 67. R. Huang, Z. a Ripstein, R. Augustyniak, M. Lazniewski, K. Ginalski, L. E. Kay, J. L.
830 Rubinstein, Unfolding the mechanism of the AAA+ unfoldase VAT by a combined cryo-
831 EM, solution NMR study. *Proc. Natl. Acad. Sci. U. S. A.* (2016)
832 https:/doi.org/10.1073/pnas.1603980113.
833 68. A. Martin, T. A. Baker, R. T. Sauer, Rebuilt AAA + motors reveal operating principles for
834 ATP-fuelled machines. *Nature* **437**, 1115–1120 (2005).
835 69. E. Gasteiger, C. Hoogland, A. Gattiker, S. Duvaud, M. R. Wilkins, R. D. Appel, A.
836 Bairoch, “Protein Identification and Analysis Tools on the ExPASy Server” in *The*

Proteomics Protocols Handbook, J. M. Walker, Ed. (Humana Press, 2005), pp. 571–607.

70. J. G. B. T.-M. in E. Nørby, "[11] Coupled assay of Na+,K+-ATPase activity" in *Biomembranes Part P: ATP-Driven Pumps and Related Transport: The Na,K-Pump*, (Academic Press, 1988), pp. 116–119.

71. C. R. Marr, S. Benlekbir, J. L. Rubinstein, Fabrication of carbon films with ~500nm holes for cryo-EM with a direct detector device. *J. Struct. Biol.* **185**, 42–47 (2014).

72. C. J. Russo, L. A. Passmore, Ultrastable gold subtrates for electron cryomicroscopy. *Science (80-.).* **346**, 1377–1380 (2014).

73. J. R. Meyerson, P. Rao, J. Kumar, S. Chittori, S. Banerjee, J. Pierson, M. L. Mayer, S. Subramaniam, Self-assembled monolayers improve protein distribution on holey carbon cryo-EM supports. *Sci. Rep.* **4**, 7084 (2014).

74. W. F. Tivol, A. Briegel, G. J. Jensen, An improved cryogen for plunge freezing. *Microsc. Microanal.* **14**, 375–379 (2008).

75. E. F. Pettersen, T. D. Goddard, C. C. Huang, G. S. Couch, D. M. Greenblatt, E. C. Meng, T. E. Ferrin, UCSF Chimera—A visualization system for exploratory research and analysis. *J. Comput. Chem.* **25**, 1605–1612 (2004).

76. R. Y. R. Wang, M. Kudryashev, X. Li, E. H. Egelman, M. Basler, Y. Cheng, D. Baker, F. Dimaio, De novo protein structure determination from near-atomic-resolution cryo-EM maps. *Nat. Methods* **12**, 335–338 (2015).

77. P. Emsley, K. Cowtan, Coot: model-building tools for molecular graphics. *Acta Crystallogr. Sect. D* **60**, 2126–2132 (2004).

78. L. A. Kelley, S. Mezulis, C. M. Yates, M. N. Wass, M. J. E. Sternberg, The Phyre2 web portal for protein modeling, prediction and analysis. *Nat. Protoc.* **10**, 845 (2015).

79. P. D. Adams, *et al.*, PHENIX: a comprehensive Python-based system for macromolecular structure solution. *Acta Crystallogr. Sect. D* **66**, 213–221 (2010).

80. V. B. Chen, W. B. Arendall III, J. J. Headd, D. A. Keedy, R. M. Immormino, G. J. Kapral, L. W. Murray, J. S. Richardson, D. C. Richardson, MolProbity: all-atom structure validation for macromolecular crystallography. *Acta Crystallogr. Sect. D* **66**, 12–21 (2010).

81. B. A. Barad, N. Echols, R. Y.-R. Wang, Y. Cheng, F. DiMaio, P. D. Adams, J. S. Fraser, EMRinger: side chain–directed model and map validation for 3D cryo-electron microscopy. *Nat. Methods* **12**, 943 (2015).

82. T. D. Goddard, C. C. Huang, E. C. Meng, E. F. Pettersen, G. S. Couch, J. H. Morris, T. E. Ferrin, UCSF ChimeraX: Meeting modern challenges in visualization and analysis. *Protein Sci.* **27**, 14–25 (2018).

83. M. Harrower, C. A. Brewer, ColorBrewer.org: An Online Tool for Selecting Colour Schemes for Maps. *Cartogr. J.* **40**, 27–37 (2003).